Strain localization in dry sheared granular materials: A compactivity-based approach

Xiao Ma* and Ahmed Elbanna
Department of Civil and Environmental Engineering, University of Illinois, Urbana-Champaign, Illinois, USA

(Received 21 March 2018; published 28 August 2018)

Shear banding is widely observed in natural fault zones as well as in laboratory experiments on granular materials. Understanding the dynamics of strain localization under different loading conditions is essential for quantifying strength evolution of fault gouge and energy partitioning during earthquakes and characterizing rheological transitions and fault zone structure changes. To that end, we develop a physics-based continuum model for strain localization in sheared granular materials. The grain-scale dynamics is described by the shear transformation zone (STZ) theory, a nonequilibrium statistical thermodynamic framework for viscoplastic deformation in amorphous materials. Using a finite strain computational framework, we investigate the initiation and growth of complex shear bands under a variety of loading conditions and identify implications for strength evolution and the ductile to brittle transition. Our numerical results show similar localization patterns to field and laboratory observations and suggest that shear zones show more ductile response at higher confining pressures, lower dilatancy, and loose initial conditions. Lower pressures, higher dilatancy, and dense initial conditions favor a brittle response and larger strength drops. These findings shed light on a range of mechanisms for strength evolution in dry sheared granular materials and provide a critical input to physics-based multiscale models of fault zone instabilities.

DOI: 10.1103/PhysRevE.98.022906

I. INTRODUCTION

Fault gouge is a highly granulated material which is formed in many fault zones due to the fragmentation of the intact host medium rocks as the fault develops under progressive shearing. Studies have shown extreme localization of slip within gouge layers that in some cases may be less than a few millimeters thick [1–6]. Origin and evolution dynamics of this shear banding at laboratory and field scales are not yet fully understood.

Strain localization in granular material has been identified and studied extensively, mostly at low strain rates, using the triaxial apparatus and direct double-shear test machines [7–12]. Localization has been cited as a mechanism for material weakening in fault zones and has been linked to strain softening and changes in frictional rate sensitivity [10]. These rheological changes play a critical role in determining the stability of sliding during nucleation and subsequent propagation of earthquakes, and they control a variety of source parameters including strength drop, slip weakening distance, and energy partitioning [9,11,13,14]. Understanding the interplay between strain localization dynamics and fault zone constitutive response is thus crucial for resolving several outstanding challenges in earthquake physics.

Strain localization in sheared fault gouge has also been studied numerically [15,16]. The focus was primarily on thermal mechanisms for strain localization including pore fluid thermal pressurization and chemical decomposition of carbonate-rich gouge due to shear heating. These models were limited to idealized one-dimensional (1D) geometry in the direction perpendicular to the mathematical fault plane. Daub and Carlson [17] and Hermundstad *et al.* [18] investigated athermal shear localization in gouges due to inhomogeneous plastic deformation. Lieou *et al.* [19] and Konik and Elbanna [20] have extended this framework to investigate the influence of grain fragmentation and acoustic vibrations on strain localization dynamics respectively. These models were also limited to 1D idealization of fault zones. Field and laboratory observations suggest that shear bands have complicated structures, including Riedel, boundary, and Y shears. Such complexity is beyond the capacity of 1D models. Here, we present a continuum two-dimensional (2D) model for strain localization in viscoplastic gouge layers to capture the evolution of this complex texture.

Our primary theoretical tool for investigating fault zone inelasticity is the shear transformation zone (STZ) framework [21]. The STZ theory is a continuum model of plastic deformation in amorphous solids that quantifies local configurational disorder [21]. The basic assumption in the theory is that plastic deformation occurs at rare noninteracting localized spots known as STZs. An internal state variable, the effective temperature, or compactivity [19,22] describes fluctuations in the configurational states of the granular material and controls the density of STZs [19]. In hard-sphere granular systems, changes in compactivity are related to the evolution of porosity [19]. This approach coarse grains granular simulations while retaining important physical concepts. The STZ framework has been recently extended to resolve several additional granular-specific mechanisms, such as grain breakage [23] and compaction under vibration [20,24], beyond what is possible using classical friction and granular plasticity laws [25,26]. Elbanna and Carlson [27] have also extended the flash heating theory [14] to fault gouge within the STZ framework.

The main contribution of this paper is the development of a thermodynamically consistent framework for amorphous plasticity in 2D finitely deformed granular media using the

*xiaoma5@illinois.edu

concept of compactivity. Compactivity was first introduced by Edwards [28] as an alternative for Gibb's temperature to describe packing of hard spheres where volume, not energy, is the relevant thermodynamic variable. Lieou and Langer [29] extended that concept to describe far from equilibrium dynamics of assemblies of hard spheres. They considered one-dimensional uniformly deformed systems. Here we extend their formulation to higher dimensions and implement it in a finite element framework, allowing for spatial heterogeneities and investigation of initiation and evolution of complex shear bands as well as changes in granular material strength with slip.

The remainder of the paper is organized as follows. In Sec. II, we review the basic elements of the STZ theory. In Sec. III, we discuss the implementation of the STZ theory into a finite strain viscoplastic finite element framework. In Sec. IV, we present our numerical results for the evolution of shear bands and factors affecting the shear band localization. In Sec. V, we discuss the implications of our findings for fault-zone dynamics and multiscale modeling of earthquakes. We summarize our conclusions in Sec. VI.

II. CONTINUUM SHEAR TRANSFORMATION ZONE (STZ) THEORY

Shear transformation zone (STZ) theory is a nonequilibrium statistical thermodynamic framework for describing plastic deformations in amorphous materials by quantifying local disorder. It has been applied to a variety of systems including granular fault gouge [17,18,30,31], glassy materials [21,32–34], thin film lubricants [35], and hard spheres [29]. The theory, with just a few parameters, has successfully reproduced a large number of experiments and molecular dynamics simulations for glassy materials, including strain localization patterns (e.g., Refs. [22,29,34,36,37]). Recently, the theory was extended to model shear flow of granular materials with breakable particles [23], incorporating flash heating effects [27] as well as acoustic fluidization under low normal stresses [38]. Furthermore, the theory has been implemented to investigate conditions for stability of sliding and strain localization in granular layers subjected to shear and vibrations [20,24] and has pointed to the possible effect of vibrations in transition from rapid slip to slow slip and eventually stable sliding; a mechanism that may play a role in tremor-slow slip interaction [24].

A basic feature of granular materials is that particles move and rearrange in response to applied stress. Molecular dynamics simulations of glassy materials [21] and discrete element models of granular materials [39] reveal that plastic irreversible deformation is concentrated in localized regions which came to be called shear transformation zones (STZs). These regions undergo slow configurational rearrangement by flipping between two orientations, antialigned and aligned with the direction of optimally oriented shear stresses [21]. This occurs on longer timescales than the scale of kinetic vibrations of the particles. Thus, the thermodynamics of the system may be described by decomposing the system into a configuration subsystem and a kinetic-vibrational subsystem, and the two are weakly coupled. A reservoir may also be introduced with which the granular system may exchange heat.

A single STZ transition is represented by an irreversible rearrangement of a cluster of particles, whereby the particles locally exchange nearest neighbor relationships. While an arbitrary motion in a granular assembly may be decomposed into affine (i.e., a linear map) and nonaffine components, it is the irreversible nonaffine rearrangements (i.e., topological changes) of the particles that characterize an STZ. The creation, annihilation, and transition of STZs may be due to mechanical forcing, acoustic vibrations, or thermal fluctuations (for nanoparticles). In this paper, we focus on athermal STZ dynamics that is mainly caused by shearing.

A state variable, the compactivity χ, is introduced to measure the degree of configurational disorder in the system and to set the number of STZs. The compactivity is formally defined as the change in the volume (per unit reference volume) V_p for a unit change in the system configurational entropy S_c: $\chi = \partial V_p/\partial S_c$ [29]. In the following subsections, we present a formulation for a compactivity-based shear transformation zone theory in a finite deformation framework.

A. Finite deformation kinematics

We introduce a continuous mapping from a reference undeformed configuration X to a current deformed configuration x:

$$\mathbf{x} = (\mathbf{X}, t). \tag{1}$$

We define the deformation gradient:

$$\mathbf{F} = \nabla \mathbf{x}. \tag{2}$$

We adopt a multiplicative decomposition of the deformation gradient [40–42] such that

$$\mathbf{F} = \mathbf{F}^e\mathbf{F}^p \quad \text{with} \quad J = |\mathbf{F}|, \quad J^e = |\mathbf{F}^e| \quad \text{and} \quad J^p = |\mathbf{F}^p|. \tag{3}$$

Accordingly,

$$J = J^e J^p. \tag{4}$$

The gradient of the velocity field is

$$\mathbf{L} = \nabla v = \dot{\mathbf{F}}\mathbf{F}^{-1}. \tag{5}$$

From Eqs. (3) and (5),

$$\mathbf{L} = (\dot{\mathbf{F}}^e\mathbf{F}^p + \mathbf{F}^e\dot{\mathbf{F}}^p)\mathbf{F}^{p^{-1}}\mathbf{F}^{e^{-1}} = \dot{\mathbf{F}}^e\mathbf{F}^{e^{-1}} + \mathbf{F}^e\dot{\mathbf{F}}^p\mathbf{F}^{p^{-1}}\mathbf{F}^{e^{-1}}$$
$$= \mathbf{L}^e + \mathbf{F}^e\mathbf{L}^p\mathbf{F}^{e^{-1}}. \tag{6}$$

We may write $\mathbf{L}^e = \mathbf{D}^e + \mathbf{W}^e$ and $\mathbf{L}^p = \mathbf{D}^p + \mathbf{W}^p$, where $\mathbf{D}$ is the symmetric component and $\mathbf{W}$ is the skew symmetric component. We further assume that $\mathbf{W}^p = 0$, and then

$$\mathbf{L} = \mathbf{L}^e + \mathbf{F}^e\mathbf{D}^p\mathbf{F}^{e^{-1}}. \tag{7}$$

B. STZ kinematics

Let the symbol α denote the orientation of an STZ, which is the orientation of the axes along which its $\pm$ states are defined as shown schematically in Fig. 1. Let $N_\pm^\alpha$ indicate the number of STZs oriented in the $+$ or $-$ states. The master rate equations for STZs could be written as

$$\tau_o\dot{N}_\alpha^\pm = R(\pm s_\alpha)N_\alpha^\mp - R(\mp s_\alpha)N_\alpha^\pm + \tilde{\Gamma}\left(\tfrac{1}{2}N^{\text{eq}} - N_\alpha^\pm\right), \tag{8}$$

where $\tau_o = a/\sqrt{P/\rho_G}$ is the inertial timescale [29] and $\tilde{\Gamma} = \Gamma + \rho$ is the attempt frequency. Here Γ and ρ denote the

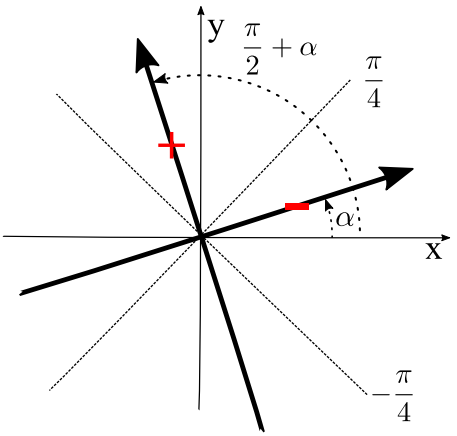

FIG. 1. Schematic drawing of an STZ transition. The STZs are classified into two states: + or −. The + state is that an STZ's angle between the direction of its elongation and the y axis is smaller than $\pi/4$. The − state is that an STZ's angle between the direction of its elongation and the x axis is smaller than $\pi/4$.

mechanical and vibration noise strengths, respectively. In this paper, we do not consider the vibration noise strengths by taking $\rho = 0$. R denotes the STZ flipping rates, and $N^{\rm eq}$ indicates the equilibrium number of STZs. The first two terms in Eq. (8) represent the process of flipping of STZs from one state to another. The third term represents the creation and annihilation of STZs.

We assume that the total plastic strain rate tensor is decomposed into deviatoric and volumetric parts as follows:

$$\mathbf{D}^p_{\rm tot} = \mathbf{D}^p_{\rm dev} + \mathbf{D}^p_{\rm vol}. \tag{9}$$

The flow direction of the deviatoric part of the plastic strain rate $\mathbf{D}^p_{\rm dev}$ must be proportional to a traceless tensor d_{ij}. For two-dimensional systems, Pechenik [43] showed that

$$d^\alpha_{ij} = 2\hat{e}^\alpha_i \hat{e}^\alpha_j - \delta_{ij}, \tag{10}$$

where $\hat{\mathbf{e}}$ is a unit vector at an angle α relative to the maximum shear stress, with $-\pi/4 < \alpha < \pi/4$. If the maximum shear stress is at an angle ϕ with respect to the axis, then $s_{ij} = \bar{s} d^\phi_{ij}$, where s is the deviatoric stress and $\bar{s} = \sqrt{s_{ij}s_{ij}/2}$ is the second invariant of the stress tensor.

The deviatoric part of plastic rate tensor D^p_{ij} is the superposition of all of the microscopic shear strain rates accumulating through the STZ transitions and may be written as

$$\tau_o D^p_{ij} = \frac{\epsilon_o}{N}\langle d^\alpha_{ij}[R(s^\alpha)N^\alpha_- - R(-s^\alpha)N^\alpha_+]\rangle. \tag{11}$$

Here, ϵ_0 is a shear increment of order unity. The angle brackets $\langle\cdot\rangle$ denote an average over STZ orientations α consistent with the $\pm$ constraints (see Ref. [43] for more details). The traceless, symmetric tensor d^α_{ij} projects these transitions onto the i, j axes. Expanding terms in Eq. (11), we obtain

$$\tau_o D^p_{ij} = \frac{\epsilon_o}{N}\left\langle d^\alpha_{ij}\left\{\frac{1}{2}[R(s^\alpha) - R(-s^\alpha)][N^\alpha_+ + N^\alpha_-] - \frac{1}{2}[R(s^\alpha) - R(-s^\alpha)][N^\alpha_+ - N^\alpha_-]\right\}\right\rangle. \tag{12}$$

We assume that $R(s^\alpha) + R(-s^\alpha)$ and $R(s^\alpha) - R(-s^\alpha)$ depend only weakly on the orientation and may be replaced by an α-independent function of the magnitude of the stress [44], We introduce the following intensive quantities:

$$\Lambda = \frac{1}{N}\int [N^\alpha_+ + N^\alpha_-]d\alpha, \tag{13}$$

$$m_{ij} = \left\langle d^\alpha_{ij}\left[\frac{N^\alpha_+ - N^\alpha_-}{N^\alpha_+ + N^\alpha_-}\right]\right\rangle, \tag{14}$$

$$\tfrac{1}{2}[R(s^\alpha) + R(-s^\alpha)] \approx \tfrac{1}{2}[R(\bar{s}) + R(-\bar{s}))] \equiv C(\bar{s}), \tag{15}$$

$$\left\langle d^\alpha_{ij}\left[\frac{R(s^\alpha) - R(-s^\alpha)}{R(s^\alpha) + R(-s^\alpha)}\right]\right\rangle \approx \frac{s_{ij}}{\bar{s}}\left[\frac{R(\bar{s}) - R(-\bar{s})}{R(\bar{s}) + R(-\bar{s})}\right] \equiv \frac{s_{ij}}{\bar{s}}\mathcal{T}(\bar{s}). \tag{16}$$

Here Λ is the total STZ density given by the total number of STZs normalized to N, where N is the total number of grains or particles in the same volume. m_{ij} is a deviatoric tensor that describe the average STZ orientation bias. The rate parameter $C(\bar{s})$ describes the flipping rate bias, and $\mathcal{T}(\bar{s})$ is the orientational rate bias.

Using the preceding definition of Λ, m_{ij}, $C(\bar{s})$, and $\mathcal{T}(\bar{s})$, we could write out the STZ governing equations:

$$\tau_o D^p_{ij} = \epsilon_0 C(\bar{s})\Lambda\left[\frac{s_{ij}}{\bar{s}}\mathcal{T}(\bar{s}) - m_{ij}\right], \tag{17}$$

$$\tau_o \dot{m}_{ij} = 2C(\bar{s})\left(\frac{s_{ij}}{\bar{s}}\mathcal{T} - m_{ij}\right) - \Gamma m_{ij} - \tau_0\frac{\dot{\Lambda}}{\Lambda}m_{ij}, \tag{18}$$

$$\tau_o\dot{\Lambda} = \Gamma(\Lambda^{\rm eq} - \Lambda). \tag{19}$$

C. Laws of thermodynamics

1. First law of thermodynamics

$$\dot{U}_{\rm int} = W_{\rm ext}. \tag{20}$$

Here, $\dot{U}_{\rm int}$ is the rate of change of the total internal energy; $W_{\rm ext}$ is the conventional external work rate due to surface traction and body forces. The internal energy may be expanded as

$$\dot{U}_{\rm int} = \dot{U}_c + \dot{U}_k + \dot{U}_R, \tag{21}$$

where U_c is the strain energy (associated with elasticity of loading device or elasticity of the particles), U_k is the kinetic-vibrational energy associated with the thermodynamics Gibbs temperature and heat flow, and U_R is the reservoir energy (assuming that the subsystem is connected to the environment and there is an exchange of heat between the two). All energies are measured per unit volume of the intermediate configuration for algebraic convenience as will be shown later.
The external work rate is given by

$$\begin{aligned} W_{\rm ext} &= \int_{\partial V}\boldsymbol{\sigma}\mathbf{n}\cdot\mathbf{v}da + \int_V \mathbf{b}\cdot\mathbf{v}dV \\ &= \int_V(\nabla\cdot\boldsymbol{\sigma})\cdot\mathbf{v}dV + \int_V \boldsymbol{\sigma}:\nabla\mathbf{v}dV + \int_V \mathbf{b}\cdot\mathbf{v}dV \\ &= \int_V(\boldsymbol{\sigma}:\mathbf{L}^e + \boldsymbol{\sigma}:\mathbf{F}^e\mathbf{L}^p\mathbf{F}^{e^{-1}})dV \end{aligned}$$

$$= \int_V (\boldsymbol{\sigma} : \mathbf{L}^e + \mathbf{F}^{e^T}\boldsymbol{\sigma}\mathbf{F}^{e^{-T}} : \mathbf{D}^p) dV$$
$$= \int_V (\boldsymbol{\sigma} : \mathbf{L}^e + J^{e^{-1}} J^e \mathbf{F}^{e^T}\boldsymbol{\sigma}\mathbf{F}^{e^{-T}} : \mathbf{D}^p) dV$$
$$= \int_V (\boldsymbol{\sigma} : \mathbf{L}^e + J^{e^{-1}}\mathbf{M} : \mathbf{D}^p) dV. \quad (22)$$

Here $\boldsymbol{\sigma}$ is the Cauchy stress, $\mathbf{n}$ is the normal direction vector to the surface, and $\mathbf{b}$ is the body force density. We have used the divergence theorem, Eq. (7), and imposed static equilibrium $\nabla \cdot \boldsymbol{\sigma} + \mathbf{b} = 0$.[1] An important result of the the above analysis is that the stress conjugated to the inelastic strain rate tensor is $\mathbf{M} = J^e \mathbf{F}^{e^T}\boldsymbol{\sigma}\mathbf{F}^{e^{-T}}$. This is a consequence of the finite deformation analysis. We may recognize this stress as the Mandel stress routinely used in plasticity theories [45]. At small elastic strain, as in this study, the Mandel stress reduces to Cauchy stress.

Assuming that an energy density exists for each of the components of the internal energy and recognizing the arbitrariness of the considered differential volume, the first law of thermal dynamics takes the following local form:

$$J^{e^{-1}}(\dot{\psi}_c + \dot{\psi}_k + \dot{\psi}_R)$$
$$= \boldsymbol{\sigma} : \mathbf{L}^e + J^{e^{-1}}\mathbf{s}^* : \mathbf{D}^p_{\text{dev}} - J^{e^{-1}} P tr\mathbf{D}^p$$
$$= \boldsymbol{\sigma} : \mathbf{L}^e + J^{e^{-1}}\mathbf{s}^* : \mathbf{D}^p_{\text{dev}} - J^{e^{-1}} P tr\mathbf{D}^p. \quad (23)$$

Here, $\mathbf{s}^*$ is the deviatoric component and P is the hydrostatic component of the Mandel stress. When we rearrange terms and account for the symmetry of the Cauchy stress $\boldsymbol{\sigma}$, the local form of the first law of thermodynamics becomes

$$\dot{\psi}_c + \dot{\psi}_k + \dot{\psi}_R = \tfrac{1}{2} J^e \boldsymbol{\sigma} : \dot{\mathbf{C}}^e + \mathbf{s}^* : \mathbf{D}^p_{\text{dev}} - P tr\mathbf{D}^p, \quad (24)$$

where $\mathbf{C}^e$ is the Cauchy-Green Strain tensor.

Constitutive equation specialization. The total entropy of the system S_{tot} is partitioned into entropy of configuration subsystem S_c (associated with the slow arrangement of the particles), entropy of the kinetic subsystem S_k (associated with the fast vibrational degrees of freedom of the particles), and the entropy of the reservoir S_R as stated in Eq. (25):

$$S_{\text{tot}} = S_c + S_k + S_R. \quad (25)$$

We may also write the energy density of the different energy components in the system as follows:

(1) The elastic strain energy density:

$$\psi_c = \psi_c(\mathbf{C}^e). \quad (26)$$

(2) The kinetic energy density:

$$\psi_k = \psi_k(S_k). \quad (27)$$

(3) The reservoir energy density:

$$\psi_R = \psi_R(S_R). \quad (28)$$

Furthermore, the plastic volumetric strain may be written as

$$V_p = V_p(S_c, \{\Omega\}). \quad (29)$$

Here Ω are STZ internal variables such as STZ density and orientations. Taking the time derivative of (29) gives

$$\dot{V}_p = \chi \dot{S}_c + \sum \frac{\partial V_p}{\partial \Omega}\dot{\Omega}. \quad (30)$$

Here we have used the definition of compactivity

$$\chi = \frac{\partial V_p}{\partial S_c}. \quad (31)$$

We may also set

$$\dot{V}^p = tr\mathbf{D}^p_{\text{tot}}. \quad (32)$$

2. *Second law of thermodynamics*

The total entropy is a nondecreasing function of time:

$$\dot{S} = \dot{S}_c + \dot{S}_k + \dot{S}_R \geqslant 0. \quad (33)$$

Using the aforementioned constitutive dependencies, the fact that $\dot{\psi}_{\mathbf{k}} = \theta_k \dot{S}_k$, where $\theta_k = \partial\psi_k/\partial S_k$ is the kinetic temperature, and the energy balance equation to eliminate S_c, the entropy rate statement reduces to

$$\left\{ \begin{array}{l} \mathbf{s}^* : \mathbf{D}^p_{\text{dev}} - P\sum \dfrac{\partial V_p}{\partial \Omega}\dot{\Omega} \\ \left(\dfrac{1}{2} J^e \boldsymbol{\sigma} - \dfrac{\partial \psi_e}{\partial \mathbf{C}^e}\right) : \dot{\mathbf{C}}^e \\ -\theta_k \dot{S}_k - \dot{\psi}_R + P\chi(\dot{S}_R + \dot{S}_k) \end{array} \right\} \geqslant 0. \quad (34)$$

To satisfy this inequality, we must have

$$\boldsymbol{\sigma} = 2J^{e^{-1}} \frac{\partial \psi_e}{\partial \mathbf{C}^e}. \quad (35)$$

We further request that dissipation is strictly non-negative:

$$\mathcal{D} = \mathbf{s}^* : \mathbf{D}^p_{\text{dev}} - P\sum \frac{\partial V_p}{\partial \Omega}\dot{\Omega} \geqslant 0. \quad (36)$$

Finally, for the reservoir and kinetic vibrational subsystems, we have

$$-\theta_k \dot{S}_k - \dot{\psi}_R + p\chi(\dot{S}_k + \dot{S}_R)$$
$$= (-\theta_k + P\chi)(\dot{S}_k + \dot{S}_R) - \dot{\psi}_R\left(1 - \frac{\theta_k}{\theta_R}\right) \geqslant 0, \quad (37)$$

where we have used the identity $\dot{\psi}_R = \theta_R \dot{S}_R$ and θ_R is the reservoir temperature. The inequality (37) may then be satisfied by taking

$$\dot{\psi}_R = -A\left(1 - \frac{\theta_k}{\theta_R}\right), \quad (38)$$
$$\dot{S}_k + \dot{S}_R = B(-\theta_k + P\chi), \quad (39)$$

where A and B are positive coefficients.

[1] We may consider inertia effects and use instead $\nabla \cdot \boldsymbol{\sigma} + \mathbf{b} = \rho\ddot{u}$. This in turn introduces an extra term $\int(\rho\ddot{u}) \cdot v dV = \frac{1}{2}\frac{d}{dt}(\int \rho v^2 dV)$. This rate of change of the kinetic energy of the propagating waves may be moved to the other side of energy balance equation to modify the energy rate of the kinetic subsystem $\dot{\psi}_k$. This will not change the remainder of the thermodynamic derivation.

Assuming that the kinetic temperature is always in equilibrium with the reservoir temperature, then

$$\dot{\psi}_R = 0, \tag{40}$$

$$\theta_k \dot{S}_k = B(-\theta_k + P\chi), \tag{41}$$

$$\dot{\psi}_k = \theta_k \dot{S}_k = B(-\theta_k + P\chi). \tag{42}$$

Substituting back into the energy balance equation, we have

$$P\chi \dot{S}_c = -P \sum \frac{\partial V_p}{\partial \Omega} \dot{\Omega} + \mathbf{s}^* : \mathbf{D}^p_{\text{dev}} - B(-\theta_k + P\chi). \tag{43}$$

Moreover,

$$\chi \dot{S}_c = \chi \left(\frac{\partial S_c}{\partial \chi} \dot{\chi} + \sum \frac{\partial S_c}{\partial \Omega} \dot{\Omega} \right) = c_o \dot{\chi} + \chi \sum \frac{\partial S_c}{\partial \Omega} \dot{\Omega}. \tag{44}$$

Using (44) in (43) yields

$$\begin{aligned} P c_o \dot{\chi} = &-P\chi \sum \frac{\partial S_c}{\partial \Omega} \dot{\Omega} - P \sum \frac{\partial V_p}{\partial \Omega} \dot{\Omega} \\ &+ \mathbf{s}^* : \mathbf{D}^p_{\text{dev}} - B(-\theta_k + P\chi), \end{aligned} \tag{45}$$

where we have introduced the parameter $\mathbf{c}_o$ to approximate $\boldsymbol{\chi} \frac{\partial S_c}{\partial \chi}$. In general, $\mathbf{c}_o$ may depend on χ but we will assume it to be approximately constant in the subsequent calculations. Furthermore, the equations governing the evolution of the set of internal variables $\boldsymbol{\Omega}$, namely (18) and (19), are stiff differential equations as they do not have a prefactor Λ, typically a very small number, compared to the equation governing the plastic strain rate (17). Thus, we may assume that the internal variables Ω evolve on a much faster timescale than the compactivity and invoke a stationarity approximation $\dot{\Omega} = 0$ as in previous work [19]. The above equation then simplifies to

$$P c_o \dot{\chi} = \mathbf{s}^* : \mathbf{D}^p_{\text{dev}} - B(-\theta_k + P\chi). \tag{46}$$

The thermal transport coefficient B may be determined from steady state condition $\dot{\chi} = 0$ and $\chi = \hat{\chi}$ uniformly:

$$B = \frac{\mathbf{s}^* : \mathbf{D}^p_{\text{dev}}}{-\theta_k + P\hat{\chi}}. \tag{47}$$

Thus we arrive at the evolution equation for the compactivity:

$$P c_o \dot{\chi} = \left(\mathbf{s}^* : \mathbf{D}^p_{\text{dev}}\right) \left(1 - \frac{-\theta_k + P\chi}{-\theta_k + P\hat{\chi}}\right). \tag{48}$$

We assume isothermic conditions and without loss of generality we take $\theta_k = 0$. Rearranging terms, we derived the compactivity evolution equation:

$$\dot{\chi} = \frac{\mathbf{s}^* : \mathbf{D}^p_{\text{dev}}}{P c_o} \left(1 - \frac{\chi}{\hat{\chi}}\right). \tag{49}$$

The above equation states that only a fraction of the external work rate $\mathbf{s}^* : \mathbf{D}^p_{\text{dev}} = s^*_{ij} D^p_{ij}$ is dissipated to increasing χ as it is driven toward its steady state value $\hat{\chi}$ [37]. This fraction is given by $1 - \chi/\hat{\chi}$. The coefficient c_o sets a scale for the amount of work required to increase the compactivity. As c_o increases, the evolution of χ slows. The steady state value of the effective temperature is rate dependent in the limit of high strain rates $\hat{\chi}(q) = A/\log(q_0/q)$, where $q = \tau_o \dot{\gamma}$ is the dimensionless strain rate [17,37,38]. However, at strain rates significantly below a critical value, given by the inverse of the inertial timescale τ_o^{-1}, this rate dependence is weak and the steady state is almost a constant χ_∞ [19,20]. For the parameters used in this paper, the critical strain rate is of the order of $10^7/\text{s}$, which is orders of magnitudes higher than the strain rate of interest here. We will therefore adopt the approximation that $\hat{\chi} = \chi_\infty$ and thus our results represent the rate-independent limit.

D. STZ isotropic plasticity model

Here we follow Pechnick [43] and Langer [44] in their formulation of the isotropic plasticity model within the effective temperature framework and adapt it to the compactivity-based formulation.

The rate of orientational bias tensor $\dot{m}_{ij}$ evolution equation (18) is a stiff differential equation, and there is no prefactor on the right-hand side to produce slow relaxation as the term Λ in the plastic strain rate D^p_{ij} governing Eq. (17). Therefore, we may set $\dot{m}_{ij} = 0$ and replace m_{ij} by its instantaneous equilibrium value for which the right-hand size of Eq. (18) vanishes. Moreover, for an isotropic system in which the only orientations are set by the stress tensor s_{ij}, we must have

$$m_{ij} \to \frac{s_{ij}}{\bar{s}} M(\bar{s}), \tag{50}$$

where $M(\bar{s})$ is the stationary solution of Eq. (18).

To make further progress in solving Eq. (18), we must constrain the expression for the mechanical noise strength term Γ. We invoke the Pechenik hypothesis [43] that states that Γ is directly proportional to the plastic work done per STZ:

$$\Gamma = \frac{\tau_0 s_{ij} D^p_{ij}}{\epsilon_0 s_0 \Lambda} = \frac{2 s_{ij}}{s_0} C(\bar{s}) \left[\frac{s_{ij}}{\bar{s}} \mathcal{T}(\bar{s}) - m_{ij} \right], \tag{51}$$

where s_0 is an as-yet-undetermined factor with the dimension of stress.

Using Eqs. (50) and (51) in Eq. (18), the stationary solution of Eq. (18), $M(\bar{s})$, is as follows:

$$M(\bar{s}) = \frac{s_0}{2\bar{s}} \left[1 + \frac{\bar{s}}{s_0} \mathcal{T}(\bar{s}) \right] - \frac{s_0}{2\bar{s}} \sqrt{\left[1 + \frac{\bar{s}}{s_0} \mathcal{T}(\bar{s}) \right]^2 - 4 \frac{\bar{s}}{s_0} \mathcal{T}(\bar{s})}. \tag{52}$$

Simplifying the above equation, we find $M(\bar{s})$ to be

$$M(\bar{s}) \to \begin{cases} \mathcal{T}(\bar{s}) & \bar{s}/s_0 \mathcal{T}(\bar{s}) < 1 \\ s_0/\bar{s} & \bar{s}/s_0 \mathcal{T}(\bar{s}) \geqslant 1 \end{cases}. \tag{53}$$

Thus, s_0 turns out to play the role of the minimum flow stress.

We now turn to Eq. (36) to discover additional constraints on our constitutive response from the dissipation inequality. If N is the total number of STZs and v_z is the excess volume per STZ, then the total volume V can be expressed as

$$V = N\Lambda v_z + V_1[S_C - S_z(\Lambda, M)], \tag{54}$$

where S_z denotes the entropy associated with the STZs. Then, from Ref. [46],

$$S_z(\Lambda, M) = N S_0(\Lambda) + N\Lambda \psi(M), \tag{55}$$

where

$$S_0(\Lambda) = -\Lambda \ln(\Lambda) + \Lambda, \tag{56}$$

$$\psi(M) = \ln 2 - \tfrac{1}{2}(1+M)\ln(1+M) - \tfrac{1}{2}(1-M)\ln(1-M). \tag{57}$$

With two internal variables STZ density Λ and STZ orientational bias tensor m_{ij}, we could rewrite Eq. (36) as

$$\mathcal{D} = s_{ij} D^p_{ij} - P\frac{\partial V_p}{\partial \Lambda}\dot{\Lambda} - P\frac{\partial V_p}{\partial m_{ij}}\dot{m}_{ij} \geqslant 0. \tag{58}$$

Using Eqs. (54), (55), (56), and (57), we write the dissipation rate $\mathcal{D}$ as

$$\begin{aligned}\frac{\tau_0 \mathcal{D}}{v_z N} =& -\Gamma P \chi \Lambda m_{ij}\frac{d\psi}{dm_{ij}} \\ &+ 2\Lambda C(\bar{s})\left[\frac{s_{ij}}{\bar{s}}\mathcal{T}(\bar{s}) - m_{ij}\right]\left(\frac{\epsilon_0}{v_z}s_{ij} + P\chi\frac{d\psi}{dm_{ij}}\right) \\ &- P\Gamma(\Lambda^{\mathrm{eq}} - \Lambda)\left\{1 + \chi\left[\ln\Lambda - \psi(M) + m_{ij}\frac{d\psi}{dm_{ij}}\right]\right\}.\end{aligned} \tag{59}$$

We could replace the m_{ij} in Eq. (59) with $\frac{s_{ij}}{\bar{s}}M(\bar{s})$:

$$\begin{aligned}\frac{\tau_0 \mathcal{D}}{v_z N} =& -\Gamma P \chi \Lambda M(\bar{s})\frac{d\psi}{dM(\bar{s})}\frac{s_{ij}s_{ij}}{\bar{s}} \\ &+ 2\Lambda C(\bar{s})[\mathcal{T}(\bar{s}) - M(\bar{s})]\left(\frac{\epsilon_0}{v_z} + \frac{P\chi}{\bar{s}}\frac{d\psi}{dM(\bar{s})}\right)\frac{s_{ij}s_{ij}}{\bar{s}} \\ &- P\Gamma(\Lambda^{\mathrm{eq}} - \Lambda)\left(1 + \chi\left\{\ln\Lambda - \psi[M(\bar{s})]\right.\right. \\ &\left.\left. + M(\bar{s})\frac{d\psi}{dM(\bar{s})}\frac{s_{ij}s_{ij}}{\bar{s}^2}\right\}\right).\end{aligned} \tag{60}$$

Since $\mathcal{D} \geqslant 0$, all three terms should be individually nonnegative. The first term is automatically satisfied as

$$\frac{d\psi}{dM} = -\frac{1}{2}\ln\left(\frac{1+M}{1-M}\right) = -\tanh^{-1}(M). \tag{61}$$

For the second term, we need

$$\mathcal{T} = \tanh\left(\frac{\epsilon_0 \bar{s}}{v_z P \chi}\right). \tag{62}$$

Recalling the definition of $\mathcal{T}$ in Eq. (16) and the symmetry of rate factors, we may assume $R(\bar{s}) = \exp(\frac{\epsilon_0 \bar{s}}{v_z P\chi})$. Thus, higher stresses activate more transitions, while higher configurational disorder is reflective of a very noisy system, thereby reducing the transition rate. Assuming that reverse STZ transitions are negligible $R(-\bar{s}) \approx 0$, we may replace $C(\bar{s}) \approx \frac{1}{2}R(\bar{s}) = \frac{1}{2}\exp(\frac{\epsilon_0\bar{s}}{v_z P\chi})$ and $\mathcal{T}(\bar{s}) \approx 1$.

The third term of Eq. (60) may be cast as $-\frac{\partial F(\Lambda, M)}{\partial \Lambda}(\Lambda^{\mathrm{eq}} - \Lambda) \geqslant 0$, assuming $F(\Lambda, M)$ represents a free-energy-like function for the configurational subsystem. Using the nonnegativity condition, we get

$$\Lambda^{\mathrm{eq}} = \exp\left[-\frac{1}{\chi} + \psi(M) - M\frac{d\psi}{dM}\frac{s_{ij}s_{ij}}{\bar{s}^2}\right] \approx 2\exp\left(-\frac{1}{\chi}\right). \tag{63}$$

The equilibrium density of STZs is given by a Boltzmann-like factor in the compactivity. Furthermore, the STZ density Λ evolves on much faster timescale relative to the compactivity χ. This may be justified by looking at the evolution equation of compactivity (49), which depends on plastic strain rate. The evolution of the latter (17) is directly proportional to STZ density while the evolution equation of Λ is not. Therefore, we can assume Λ to be always at their instantaneous equilibrium values:

$$\Lambda = \Lambda^{\mathrm{eq}} = 2\exp\left(-\frac{1}{\chi}\right). \tag{64}$$

Now we could derive the final form of the plastic strain rate tensor

$$\tau_0 D^p_{ij} = \frac{1}{2}\epsilon_0 R(\bar{s})\Lambda^{\mathrm{eq}}\frac{s_{ij}}{\bar{s}}[1 - M(\bar{s})]. \tag{65}$$

Expanding the expression for $M(\bar{s})$ and substituting the expression for $R(\bar{s})$, $\mathcal{T}(\bar{s})$, and Λ^{eq}, we have

$$D^p_{ij} = \begin{cases}\tau_0^{-1}\epsilon_0 \exp(-1/\chi)\exp\left(\frac{\epsilon_0\bar{s}}{v_z P\chi}\right)\left[1 - \frac{s_0}{\bar{s}}\right]\frac{s_{ij}}{\bar{s}} & \bar{s} \geqslant s_0 \\ 0 & \bar{s} < s_0\end{cases}, \tag{66}$$

where s_0 is the minimum flow stress. The above formula indicates that no plasticity occurs if $\bar{s} < s_0$. Thus, it is possible to interpret $\bar{s} = s_0$ as the initial (local) yield surface equation. The value of s_0 is a function of many system variables including the grain shape, surface roughness, contact temperature, etc. Here we assume s_0 to linearly depend on the first invariant of the stress tensor I_1 as commonly observed in frictional geological materials. That is, we define $s_0 = \alpha_1 - \alpha_2 I_1/3$, in which α_1 is the cohesion of material and α_2 is the tangent of the internal friction angle of the material [47]. The assumption we are making here is that there is no plastic flow when the stress level is lower than the stress threshold should be considered as only an approximation. In future work, we plan to expand the model to incorporate more physical processes that enable plastic flow below the stress threshold. This includes for example, creep [27], acoustic vibrations [19,20], and granular fluidity [48,49]. For example, it was shown previously that acoustic vibrations may tend to fluidize the granular system, analogous to temperature effects in glasses, and enable plastic flow at stresses less than the mechanical minimum flow stress [20,38].

The volumetric strain rate is directly proportional to the rate of compactivity. As stated in Eq. (44), with the assumption that $\dot{\Lambda} = 0$ and $\dot{m}_{ij} = 0$,

$$\dot{V}_p = \frac{\partial V_p}{\partial S_c}\frac{\partial S_c}{\partial \chi}\dot{\chi} = \chi\frac{\partial S_c}{\partial \chi}\dot{\chi} = \alpha_{\mathrm{eff}}\dot{\chi}, \tag{67}$$

where α_{eff} is an effective volume expansion coefficient. Assuming volumetric deformation to be isotropic, the inelastic volume strain rate tensor is given by

$$\mathbf{D}^p_{\mathrm{vol}} = \alpha_{\mathrm{eff}}\dot{\chi}\mathbf{I}. \tag{68}$$

Here, $\mathbf{I}$ is the identity tensor.

III. NUMERICAL IMPLEMENTATION

We implement the STZ constitutive model within a finite deformation finite element framework provided by Moose

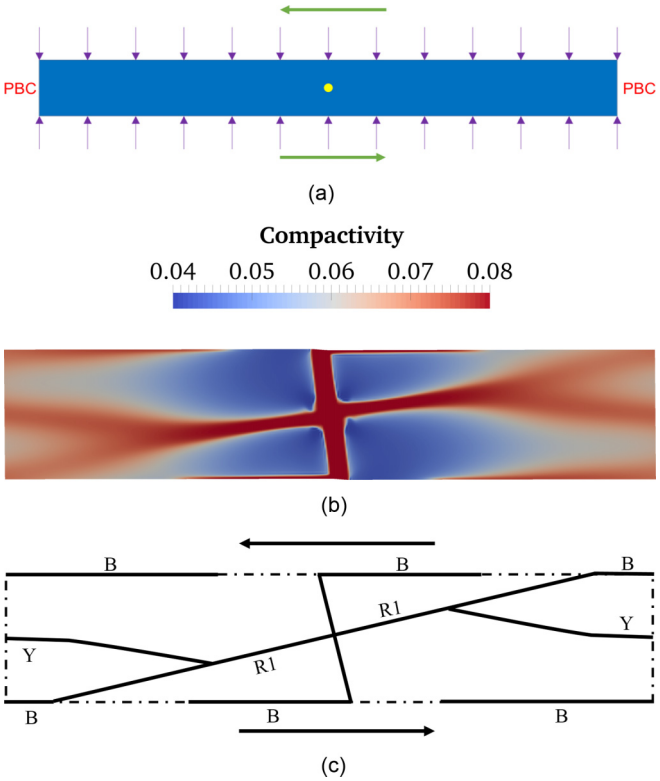

FIG. 2. (a) The setup of the simulated gouge layer. The layer is 2.0 m long and 0.2 m wide. Pressure is applied on the top and bottom surfaces. Shear loading is applied on the top and bottom boundaries. The shear loading is left lateral as indicated by the green arrow. Periodic boundary conditions are imposed on the lateral edges. The yellow circle is an inclusion introduced to trigger localization by having a higher initial compactivity than the background fault gouge (indicated by blue color). (b) The distribution of compactivity at steady state from the numerical simulation. In particular, the numerical simulations generically capture the $R1$, Y, and boundary shear bands. The results have qualitative agreement with results in Ref. [9]. (c) A schematic drawing illustrating the distribution of shear bands ($R1$, Y, and boundary shear bands) from the numerical simulations. B, boundary shear band; Y, Y shear band; R1, $R1$ shear band (simulation parameters: $\chi_o = 0.04$, $c_o = 0.025$, $P = 10$ MPa).

platform from Idaho National Laboratory. The Multiphysics Object-Oriented Simulation Environment (Moose) [50] provides a flexible platform to solve multiphysics problems implicitly and in a tightly coupled manner on unstructured meshes. The Moose framework is built on top of libraries including the Libmesh finite element library [51] and PETSc solver library [52]. The solution of the nonlinear equations of motion (dynamic equilibrium) is done using Jacobian-Free Newton-Krylov (JFNK) approach [53]. The algorithm for the plastic strain rate and stress update (material model update) is summarized in the appendix.

Model setup

We consider a layer of granular materials sheared between two parallel planes and subjected to a constant pressure at the top and the bottom as shown in Fig. 2(a). To mimic an infinite long strip, periodic boundary conditions are enforced at the left and right boundaries. At the center of the granular material, we introduce a perturbation in the local disorder by defining a circular inclusion with higher initial compactivity (i.e., less dense) than the surrounding bulk. To ensure the quality of the solution, an h-refinement study has been conducted to verify convergence with increasing resolution. The material properties that are used in the simulation are summarized in Table I.

The loading in each simulation is a two-stage process. In the first loading step, we solve a static equilibrium problem for the applied pressure at the top and bottom (assuming periodic boundary conditions at the sides). Then we apply the shear loading. To achieve a constant strain rate, we adopt a ramp loading technique in which we change the strain rate from zero to the prescribed constant value over a finite period of time using a fifth order of polynomial in time. This ensures a smooth profile for the displacement, velocity, and acceleration at the top and bottom boundaries throughout the loading history. Since our simulation is fully dynamic, this ramping reduces the effect of waves that may be generated due to an abrupt change in the loading rate during the elastic regime. We assume periodic boundary conditions for the compactivity on the lateral sides and zero flux condition across the top and bottom boundaries of the granular layer.

IV. RESULTS

A. Generic shear band localization

With the circular inclusion having a slightly higher compactivity than the rest of the granular layer, plasticity starts in that zone first. Because of the interdependence between the compactivity and inelastic strain rate [Eqs. (49) and (66)], this positive feedback causes localization of the plastic deformation in the inclusion and favors the regions in its immediate vicinity to accommodate further inelasticity. This leads to the nucleation of shear bands from the circular inclusion and their subsequent growth. As shown in Fig. 2(b), the resulting localization pattern, as measured by the distribution of the compactivity, agrees well with the schematic describing field observation as summarized in Ref. [9]. In particular, our numerical results capture the Riedel "R1" boundary and Y bands.

To further explore the relation between the stress slip response and shear bands propagation, we show in Fig. 3 the evolution of the localization patterns and its correlation with different stages in the stress slip plot. Initially, the response of the layer is elastic. With the initiation of plasticity in the central inclusion, the global response does not change much. However, with progressive shearing, the region with inelastic strain grows and diagonal bands start to propagate. With the localization of plastic deformation in the growing shear bands, the local inelastic strain rate increases causing the initiation of strain softening. This continues as the diagonal bands (primary and secondary R bands) propagate toward the top and bottom boundaries of the sample where new boundary bands start to develop. As the stress response approaches the steady state, the through-going Y band becomes more visible. Interestingly, the Y band seems to emanate from the primary Riedel shear band by curving out of it at some point during the

TABLE I. List of parameters used in the simulations for the default case. Simulations with different initial compactivity χ, confining pressure P, and the effective heat capacity c_o were also carried out and are indicated in the respective sections.

Symbol	Description	Value	Remark
E	Young's modulus	7 GPa	Range: 100 MPa (loose aggregate)–70 GPa (grain scale)
ν	Poisson ratio	0.4	Range: 0.2–0.45 [100]
h	Layer thickness	0.2 m	Arbitrary
w	Width of the granular material	0.2 m	Arbitrary
α_1	Cohesion	0.0	Neglect cohesion
α_2	Tangent of the internal friction angle	0.6	Typical value for sand (www.geotchdata.info)
ρ	Material density	1600 kg/m^3	[95]
ϵ	STZ plastic strain	1.0	Corresponding to a particle sliding a distance equal to its diameter
c_o	Effective volume capacity	0.025	Range for dilative materials: 0.001–1.0 leading to volumetric strains between 0.01 and 10% [19]
α_{eff}	Effective volume expansion coefficient	0.025	Taken as same value as c_o
$\hat{\chi}$	Steady state dimensionless compactivity	0.08	Material system specific May be adjusted to fit experiments on steady state dilation [19,101]
χ_o	Initial compactivity	0.04	Depends on initial preparation Adjustable parameter [19]
a	Grain size	1.0×10^{-4} m	Constrained by sample particle size distribution
P	Confining pressure	10 MPa	Constrained by experiments or depth

softening stage before becoming fully developed. This picture of the stress slip response alongside the compactivity evolution and localization bands development agrees qualitatively with the experimental observations of strength and microstructure evolution discussed in Ref. [10].

B. Factors affecting shear localization

1. The effect of dilatancy

One relevant feature in the STZ formulation is that the inelastic dilatancy coefficient is not prescribed, but to show

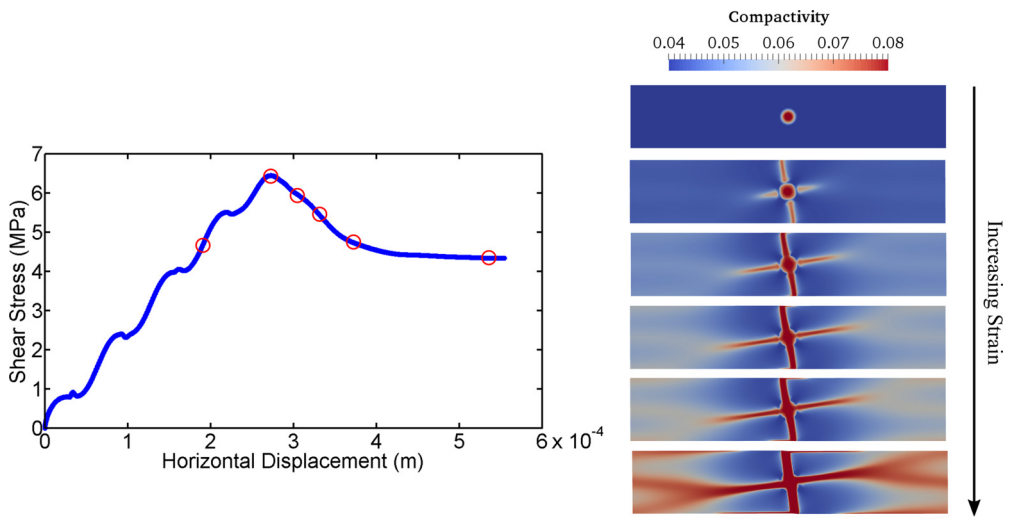

FIG. 3. Fault gouge strength evolution and the shear band formation. (a) Stress slip response. (b) The distribution of compactivity at successive time steps corresponding to the order of the red circles on panel (a). At first, the specimen is deforming elastically. With the initiation of the shear band from the center inclusion, diagonal bands start to form, and grow to the upper and lower boundary forming the Riedel shear bands, and then the primary Riedel shear band bifurcates to Y bands which fully develop near steady state. (Simulation parameters: $\chi_o = 0.04$, $c_o = 0.025$, $P = 10$ MPa.)

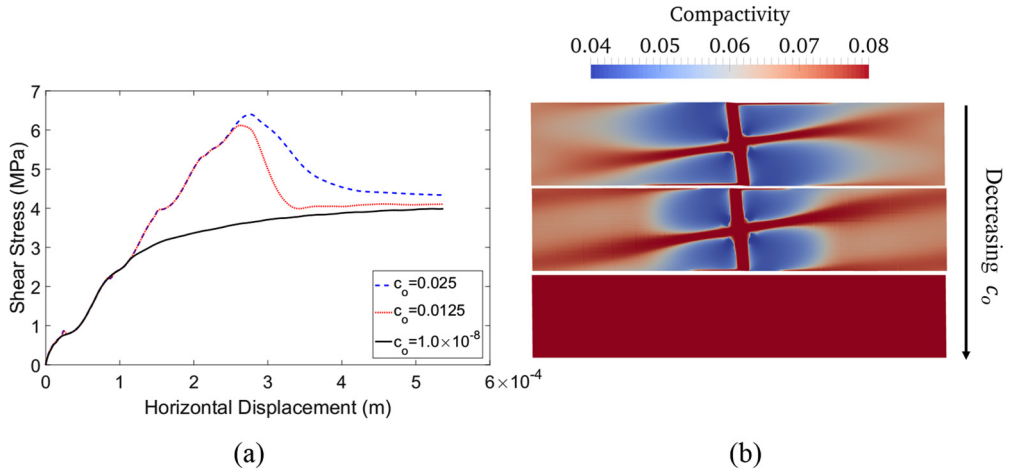

FIG. 4. Dilatancy effect on strength evolution and strain localization. (a) The stress slip response for different c_o. (b) Distribution of compactivity χ for different c_o at final slip. With decreasing value of c_o, the specimen shows a ductile behavior with no noticeable strain localization is formed when c_o is negligible. (Simulation parameters: $\chi_o = 0.04$, $P = 10$ MPa.)

this let us consider the theory formulation in a homogeneous 1D setting. The evolution of the compactivity reduces to $\dot{\chi} = \frac{s\dot{\gamma}}{c_o P}(1 - \chi/\hat{\chi}) = \frac{\dot{V}}{\alpha_{\text{eff}}}$. It follows that the dilatancy parameter is given by $\beta = \frac{\dot{V}}{\dot{\gamma}} = \frac{\alpha_{\text{eff}}}{c_o}(1 - \chi/\hat{\chi})\mu$, where $\mu = s/p$. Thus, the dilatancy evolves as a function of stress, pressure, and disorder. In the absence of additional constraints, we hypothesize that α_{eff} and c_o are of the same order of magnitude and we take them to be equal.

We vary c_o to investigate the effect of inelastic dilation on the stress slip response and shear band evolution. The results are shown in Fig. 4. As the value of c_o increases, the compactivity increases more slowly, the peak stress increases, and more localization is observed. This behavior is characteristic of dilatant media. On the other hand, if c_o becomes small enough, the inelastic dilatancy is negligible and occurs almost instantaneously, and the subsequent response becomes more ductile-like with no noticeable strain localization.

2. *The effect of ramping protocol (inertia effect)*

In this section, we investigate the possible inertia effects induced by ramping the shear loading differently from the default case. We keep the steady-state imposed strain rate value constant and a fifth-order polynomial is used for strain rate interpolation but we progressively increase the time period over which the ramping occurs. As shown in Fig. 5, with the increase of the ramp loading period, the shear band is more distributed, and the Y band development is less distinct than in the default case. Furthermore, with increasing the ramping time, the elastic regime becomes smoother due to the absence of the small stress perturbations carried by the propagating waves. The

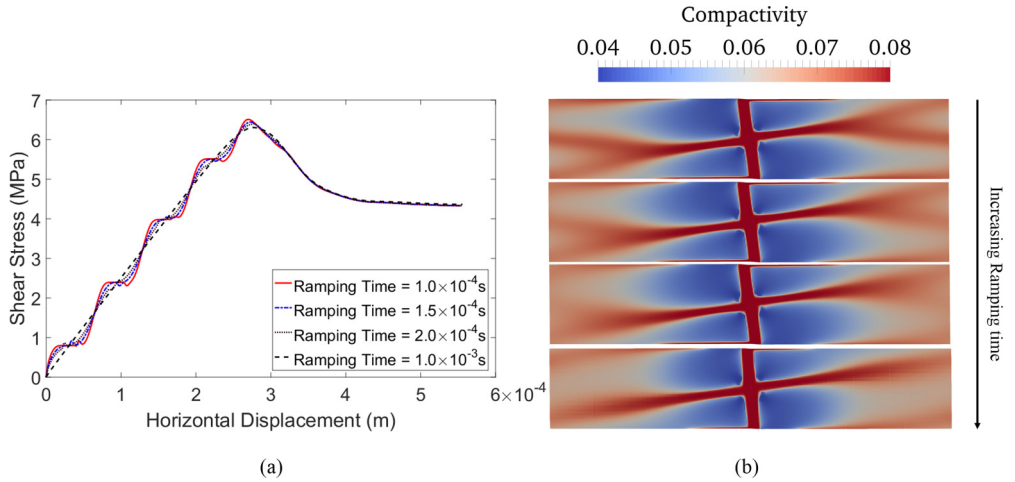

FIG. 5. Effect of ramping rate on the shear localization. (a) The shear stress slip curve with different ramping time of the imposed strain rate (steady state value = 4/s). (b) The corresponding distribution of compactivity at final slip. With shorter ramping time, the bifurcation from Riedel band to Y band is more observable. Longer ramping time causes smoother elastic response and the Y shear band is not as well developed as with the small ramping time. (Simulation parameters: $\chi_o = 0.04$, $\chi_o = 0.04$, $P = 10$ MPa.)

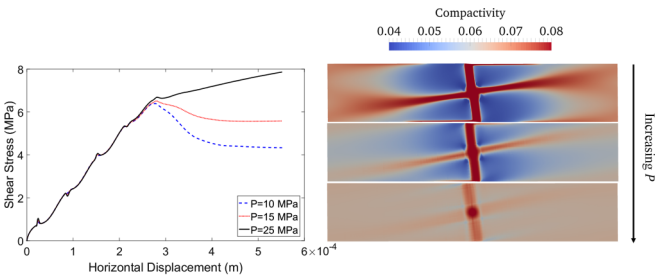

FIG. 6. Effect of confining pressure on shear localization. (a) Shear slip response with different confining pressure values: 10, 15, and 25 MPa. With increasing pressure, the peak and flow stress increase while the strength drop decreases. (b) The compactivity distribution for the different confining pressure at the final slip. From top to bottom, the confining pressure is increasing. The plasticity is distributed across the sample at higher pressure while the strain is more localized in bands at lower pressures. (Simulation parameters: $\chi_o = 0.04$, $c_o = 0.025$.)

results suggest that while the inertia effect does not change the overall qualitative features of the strain localization pattern, the Y band is more mature under quicker ramping. A possible explanation for this is that under quicker ramping, waves emanate from the top and bottom boundaries and interfere constructively in the middle of the layer causing stronger localization. This may have implications for coseismic strain localization in which the strain rates increase rapidly at the rupture tip, possibly favoring the Y band formation more. The growth of the reversed diagonal band is not visibly affected by the ramping rate.

3. *The effect of confining pressure*

In this section, we vary the applied confining pressure P on the top and bottom of the fault gouge specimen, and study its effect on strength and shear and evolution. Figure 6 shows that with the increasing confining pressure, the specimen exhibits a brittle to ductile transition. We define a brittle behavior by the existence of a strength drop and localized deformation, whereas in ductile response these features are absent. The observed transition as a function of pressure may be explained as follows. At higher pressures, the minimum flow stress s_o increases. This delays the initiation of plasticity and increases the peak stress as well as the steady state flow stress. However, with increasing pressure, the characteristic time scale for STZ transition τ decreases [Eq. (66)], enabling faster accumulation of inelastic strains and disorder (similar to the effect of reducing c_o discussed previously). At low pressure, the plasticity accumulates slowly, causing the stress to peak followed by strain softening and brittle behavior. At high pressure, the plasticity accumulates quickly after its initiation and is distributed across the layer, leading to gradual saturation of the strength without any softening signatures. This is also reflected in the compactivity plots where strain localization is evident at low pressures but shear bands are diffusive and distributed across the sample width at higher pressure.

4. *The effect of initial compactivity*

The initial preparation of the sample may affect its subsequent response. In another amorphous system, namely bulk metallic glasses, it was shown that a well-aged sample exhibits a brittle response, whereas a more disordered sample exhibits a ductile response [54]. A similar observation has been documented for granular materials where the initial relative density plays a similar role to the degree of aging. That is, an initially dense sample exhibits a brittle response, whereas an initially loose sample is ductile [10,55–58].

Here, we examine the effect of initial disorder on the brittle to ductile transition in sheared confined layers. We consider two cases: one with the default background compactivity $\chi = 0.04$ and the other with higher initial background compactivity $\chi = 0.06$ (closer to steady state value of 0.08). The results are shown in Fig. 7, where we plot the stress strain response as well as snapshots of the final compactivity distribution. For higher initial compactivity, and despite the existence of the central inclusion, it is more favorable for the sample to distribute plastic strain across the whole layer. Even if the inelastic deformation starts from the central inclusion, the disorder is

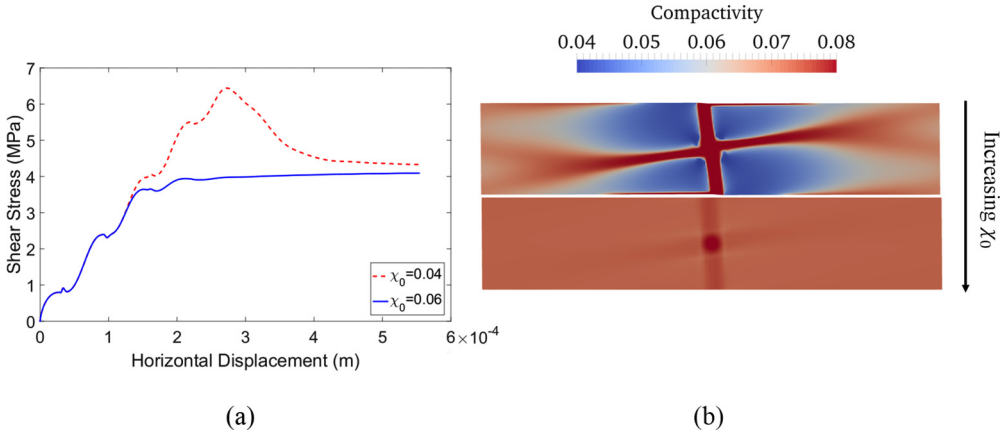

FIG. 7. Brittle to ductile transition as a function of initial compactivity. (a) Stress slip response with different initial compactivity χ_o. (b) The distribution of compactivity at steady state. With lower initial compactivity, the response is brittle with strain localization softening. (Simulation parameters: $c_o = 0.025$, $P = 10$ MPa.)

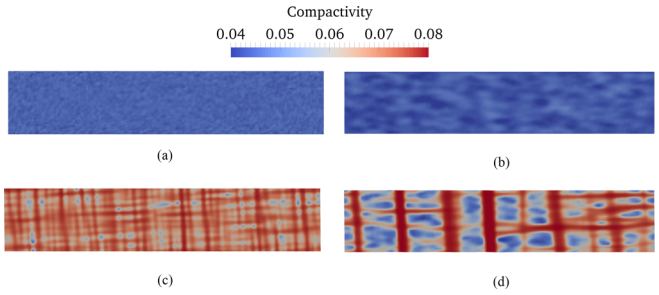

FIG. 8. Strain localization for random initial compactivity generated using Gaussian filter of width F in the Fourier domain (see text for explanation). (a) The initial random compactivity distribution with $F = 100$. (b) The distribution of compactivity at the steady state with $F = 100$. The random initial compactivity lead to a complex network of shear bands. More shear bands with small thickness are formed with smaller correlation value. (c) The initial random compactivity distribution is uniformly distributed with $F = 5$. (d) The distribution of compactivity at the steady state for $F = 5$. With larger correlation length, the shear band formation are more distinct into several major shear bands. (Simulation parameters: $\chi_o = 0.04$–0.05, $c_o = 0.025$, $P = 10$ MPa.)

high enough everywhere to accommodate plasticity shortly after. This leads to a ductile behavior in the sense that the stress progressively increases toward steady state without exhibiting a peak or strain softening. Furthermore, the plastic deformation is well distributed across the layer with no visible localization. On the other hand, with lower initial compactivity, the behavior is brittle. The inelastic deformation is localized in the center inclusion and the shear bands that grow and propagate out of it. The stress peaks at a certain slip and then goes through strain softening phase before eventually reaching a steady state value.

Compactivity χ is related to porosity [19] and changes in compactivity relate to changes in pore volume as discussed earlier (assuming incompressibility of the granular particles). Higher initial compactivity corresponds to higher initial porosity. Thus, our results suggest that initially dense layers exhibit brittle response while an initially loose layer exhibit a ductile one. The brittle to ductile transition as a function of initial preparation agrees with some experimental observations [59].

We have also tested the response corresponding to a random distribution of the initial compactivity. The random fields have spatial correlations represented by a Gaussian function in the Fourier space with different widths of the frequency filter F. We construct these random fields as follows. We first generate a normal random distribution (pure white noise) and apply a Fourier transformation to it. Next, in the frequency domain, we apply the Gaussian filter with certain width F. A smaller F value corresponds to longer spatial correlations. Then, we apply an inverse Fourier transformation on the filtered field and take the real part of the solution for the random field in space. By varying the F value, we could test different initial field correlation effects on the material behavior. Here we show two cases with $F = 100$ and $F = 5$. In both cases, the initial random compactivity is between 0.04 and 0.05. The results are shown in Fig. 8. The localization pattern is richer than the default case and exhibit more complexity. Conjugate shear bands emanate from multiple nucleation sites and interact with each other, resulting in a complex localization texture.

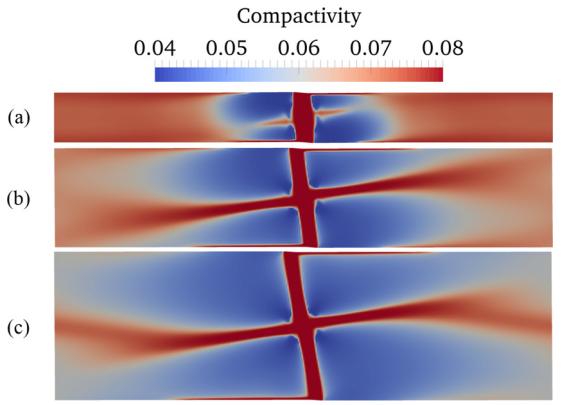

FIG. 9. Effect of layer thickness on shear localization. (a) Thickness $h = 0.1$ m: the shear bands fully saturate the layer and no distinct Riedel band is formed. (b) Thickness $h = 0.2$ m: The Riedel band forms as well as boundary shears. The Y band starts to develop. (c) Thickness $h = 0.3$ m: The Y band bifurcates at an earlier stage compared to case (b) with less visible boundary shears. (Simulation parameters: $\chi_o = 0.04$, $c_o = 0.025$, $P = 10$ MPa.)

This pattern is qualitatively similar to the localization bands observed in experiments on analog materials as well as in natural fault zones [9,57,60]. With small value of F, the random field for the initial compactivity is more spatially correlated, and more major shear band with larger thickness are formed. With large value F, the random field for initial compactivity is less spatially correlated, and a large number of small thickness conjugate shear bands is formed. The initial conditions may be tuned to generate a wide variety of localization patterns. The influence of different initial conditions on shear band dynamics and establishing a link between the Gaussian filter width and the characteristics of the microstructure [61] will be a focus of a future investigation.

5. The effect of layer thickness

It is natural to expect that the localization pattern depends on the layer thickness since the shear band has a finite length scale and for narrow enough layers, boundary interactions become important. We investigate the evolution of shear bands for three values of the layer thickness: 0.1, 0.2, and 0.3 m, sheared at the same loading velocity. As shown in Fig. 9, for the smallest thickness, the inelastic deformation almost fully saturates the layer and there is no distinct Riedel band. At intermediate thickness, there is more space for the Riedel band to grow and reach the boundary. The Y band also starts to develop. Boundary interactions still exist as evident by the development and growth of boundary shears at the right bottom and top left edges. For the largest thickness considered, the Y band bifurcates at an earlier stage. The Riedel shear continues to grow toward the boundaries. However, the development of the boundary shears is delayed due to the absence of interaction of the boundaries with either the central inclusion or the Riedel bands.

6. The effect of size of the perturbation

The size of the inclusion representing the initial perturbation in the compactivity distribution is an important length scale that

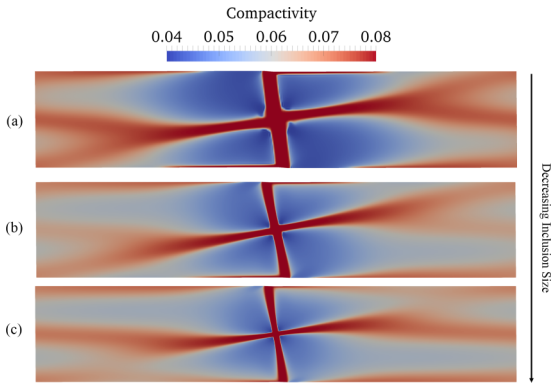

FIG. 10. Effect of inclusion size on shear localization. (a) The radius of the inclusion circle $r = 0.02$ m. (b) The radius of the inclusion circle $r = 0.01$ m. (c) The radius of the inclusion circle $r = 0.005$ m. With smaller inclusion size, the shear band is the thinner. (Simulation parameters: $\chi_o = 0.04$, $c_o = 0.025$, $P = 10$ MPa.)

contributes to determining the shear band thickness. We have run simulations with different radii of the central inclusion: 0.005, 0.01, 0.02 m. As shown in Fig. 10, as the radius of the inclusion decreases, the thickness of the shear band emanating from the inclusion also decreases. However, the shear band broadens as it propagates due to the nature of the steady state of compactivity in our model. Since we have assumed that the steady-state compactivity is constant, accommodation of increasing plastic slip is only possible through increasing the width of the shear bands, which allows accumulation of more plastic strain and strain rate.

V. DISCUSSION

Understanding deformation and failure in granular materials is a problem of both fundamental importance and practical relevance. This is because many natural phenomena as well as industrial processes are controlled by the physics of granular deformation. Earthquakes, and landslides, as well as pouring, transportation, and mixing in food and pharmaceutical industries are just few examples where granular rheology, especially that which involves the shear response due to local particle rearrangement, is of direct relevance. In many circumstances, the granular deformation is not macroscopically uniform but localizes in shear bands. This is particularly the case for crustal faults in which ample evidence exists that coseismic deformation localizes in thin regions within broad damage zones [14]. In this paper, we presented a numerical model for the evolution of viscoplastic deformation in a sheared granular layer under constant pressure with spatially heterogeneous porosity-like parameter. Using the model, it was possible to investigate the strength evolution and shear band development under different loading conditions.

The viscoplastic formulation adopted here is based on the shear transformation zone (STZ) theory, a nonequilibrium statistical thermodynamic framework for describing rate dependent inelastic deformation in amorphous materials. The STZ theory belongs to the broader class of constitutive laws with internal state variables [62]. Only the initial yield surface is defined but subsequent hardening or softening is computed as part of the solution by integrating the evolution equations of the internal variables. There have been prior fundamental work for investigating localization and plasticity in pressure-sensitive materials (see, for example, Refs. [63–68]). Most of the prior work has implemented phenomenological constitutive models. One point of departure in the current work is that the primary internal variable, the compactivity, has a clear interpretation as a measure of local disorder in the system and possesses a formal connection to fundamental thermodynamic quantities such as volume and entropy. Furthermore, the flow rule in the STZ formulation is consistent with a microscopic picture of transition dynamics of defects (STZs flipping and sliding). These features make the STZ distinct from other widely used plastic models such as Cam-Clay, Mohr-Coulomb, and Drucker-Prager models and enable direct connection with small-scale molecular dynamics or discrete element models.

A widely used constitutive model for friction in rocks and granular materials is the rate and state law [25,26]. Despite its phenomenological nature, the rate and state formulation has led to significant progress in describing several sliding phenomena particularly in bare rock surfaces experiments. The inclusion of the slip rate history, through state variables, in addition to the instantaneous slip rate in evaluating the friction coefficient has been a leap forward from earlier friction laws (see, for example, the discussion in Ref. [69]). However, the lack of physical interpretation of the state variables in the Dieterich-Ruina laws limits their predictive capability especially when it comes to gouge layers. While in principle it is possible to include more than one state variable to capture increasingly complex behavior, constraining the evolution equations of these internal variables is not straightforward. An advantage of the STZ theory in that context is that it is based on the laws of thermodynamics and the state variable evolution is constrained by energy flow and entropy evolution. In the past few years, the STZ framework has been successfully extended to incorporate physical phenomena critical for gouge mechanics such as grain fragmentation [23], flash heating [27], dilation, and compaction under combined shear and vibration [19,24,38]. Furthermore, extending STZ theory to higher dimensions (2D and 3D) is possible, enabling investigation of strain localization and inhomogeneous plastic deformation. It is not obvious how the rate and state friction may be consistently generalized to higher dimensions, despite some prior notable attempts (e.g., Ref. [70]).

While the STZ theory provides a powerful framework for describing the multiphysics of spatially extended gouge layers, the physics-based nature of the theory comes at a price: There are more parameters to be constrained in the STZ theory than in the rate and state framework. Fortunately, many of these parameters may be constrained based on physical arguments or from classical experiments. For example, Daub and Carlson [17] have shown, using a simple block slider setup, that it is possible to derive quantities analogous to the direct effect, slip evolution distance, and rate sensitivity parameter, by taking various partial derivatives of the STZ equations at both the transient and steady state limits with respect to strain rate. Using this procedure, experiments like velocity stepping as well as slide-hold-slide tests may be used to constraint several

STZ parameters. Other parameters may be freely adjusted to fit experimental observations (see Table I) or derived directly from subscale discrete element models.

The theoretical basis of the STZ framework makes it also possible to connect to more detailed microscopic models such as molecular dynamics and discrete element models. Many experiments and numerical simulations have been done to study the behavior of the glassy material [11,54,71,72]. Different approaches in modeling the plasticity in amorphous systems have also been proposed, including soft glassy rheology [73], free volume model [74–76], granular fluidity [48,49], discrete STZ approach [77], and hierarchical continuum-discrete models [78]. Recently, molecular dynamics simulations of glassy systems have made significant progress in identifying STZs using analysis of soft modes [79] or susceptibility of molecular clusters to yielding [80]. By counting the number of STZs in a given volume, the effective temperature may be directly computed using the Boltzmann distribution in STZ density. Thus, a quantitative measure of the effective temperature may be established. Furthermore, microscopic models may help in constraining parameters in the rate factors as well as those connecting the compactivity and volume changes (dilatancy). In principle, it may be possible to do more detailed studies using subscale discrete element models that communicate with the quadrature points of our finite elements. This integrated approach will provide a truly multiscale and predictive formulation for gouge deformation and is a candidate for future work.

The STZ formulation does not just compare well to rate and state friction in capturing basic features of sliding response [17] but it may also highlight additional physics that may help modify the rate and state laws. For example, the internal state variable in the STZ formulation, the compactivity, is driven by the inelastic work rate and not only by the slip (or strain) rate as in the classical evolution laws for the rate and state friction. The dependence of the compactivity on the work rate follows directly from the first law of thermodynamics and suggests that the evolution of the state variable should depend on the stress as well as the strain rate. This remains to be tested in friction experiments by carrying stress stepping tests in addition to velocity stepping ones. Furthermore, there has been some previous notable attempts for incorporating porosity evolution in the classical rate and state law and accounting for inelastic dilatancy [81,82]. In this prior work, the dilatancy factor was assumed to be constant. In the current work, the dilatancy evolves as part of the solution and depends on pressure, stress, and disorder.

In this paper, we have investigated stress slip response and shear band evolution in sheared granular layers under different conditions of confining pressure, dilation, and loading rates. We have shown that our numerical predictions agree qualitatively with many generic features of gouge deformation reported laboratory and field observations such as different shear band orientations, brittle to ductile transition with increasing confining pressure, brittle to ductile transition as a function of initial porosity, and increase in the peak strength with increased dilatancy. However, the range of parameters explored here was rather limited. For example, the confining pressure was increased only from 10 to 25 MPa. Strain rates were imposed at 4/s. Seismogenic conditions may require testing gouge response up to hundreds of MPa of confining pressure and at strain rates up to 100 or 1000/s. The range of parameters considered in this study is thus closer to experimental conditions than to field conditions. Although our model is continuum in nature, it is computationally intensive. Higher strain rates and higher pressures (which decreases the inertia timescales) require use of finer spatial meshes, smaller time steps, and high-performance computing platforms. Extension to high pressures and strain rates will be the focus of future investigations.

In this paper, we have adopted a constant value for the steady state compactivity. This results in a regularization of the strain localization mechanism as it forces the shear band to get wider to accommodate more plastic slip. While this may be justified by the fact that the strain rates considered in this study are orders of magnitude smaller than those where granular inertia lead to significant rate strengthening effects, we would like to note that other scenarios for shear band width variation may be physically plausible. For example, nonlocal effects due to acoustic vibrations or granular fluidity may further diffuse the shear band and broaden it [20,83]. On the other hand, thermal effects due to shear heating of fluids or flash heating at grain contacts [14,27] may lead to rate-dependent thinning in the shear band thickness and extreme localization. The competition between these different physical mechanisms is a topic worthy of future investigation.

In this study, we have considered an isotropic formulation of plasticity. No *a priori* constraint has been imposed on the transition kinematics of the STZs and thus there were no preferred slip directions. The pressure dependence of the response in this case originates from its influence on the volumetric strain. However, several observations exist suggesting that shear bands in geological materials as well as bulk metallic glasses may form in a preferential direction and show asymmetry between compression and tension [84–88]. Prior work [89,90] has accounted for this phenomenologically by incorporating explicitly preferred slip plane directions in the formulation of the plastic strain rate tensor. A more physics-based approach is still needed in which the anisotropy of the fabric (shape of the granular particles) is incorporated and leads to a bias in the STZ orientations. Some prior work has made progress in this direction by using an extra state variable to account for the particle shape [24]. A more fundamental approach will introduce direction-dependent transition probabilities, i.e., direction-dependent R factor, in the plastic strain rate expression and relax the proportionality between the STZ orientational bias tensor and the deviatoric stress.

In the past three decades, significant progress has been achieved in testing gouge layers at different pressures and loading rates. However, challenges still exist when it comes to mimicking conditions prevailing during earthquakes. For example, the increase in temperature at large slip velocities and pressures may melt the machine rim. Also, it is hard to confine the gouge layer at high slip rates. Furthermore, most high-speed frictional experiments are of the rotary type [91–94]. This prevents capturing physics associated with rupture propagation or inhomogeneity of slip conditions. The model explored in this study will contribute to closing this knowledge gap. By extending prior work that has been

done in the context of the 1D shear zone, through including additional physics related to grain fragmentation [23], flash heating [27], and pore fluid pressurization [16] to the current 2D viscoplastic formulation, it will be possible to predict gouge response under extreme conditions, capture extreme localization, and investigate competition between gouge dilatancy (captured in the current model) and pore fluid thermal pressurization.

In this paper, we have considered dry granular layers as a first step. Given that most fault zones are fluid infiltrated, it is important to couple the current viscoplastic formulation with an equation for pore fluid pressure evolution in response to gouge volume changes. Furthermore, at high strain rates, shear heating will be high enough to cause constrained expansion of pore fluids leading to thermal pressurization. Future work will focus on integrating temperature and pore pressure evolution in the current model. Moreover, our recent work [20,24,38], inspired by experiments of Ref. [95] and discrete element models of Ref. [96], suggest that acoustic vibrations may cause transient compaction, alter the stability of sliding in frictional fault gouge, trigger slip, and cause strain delocalization. Extending these results to higher dimensions (2D and 3D) will allow exploration of the effect of vibrations on slip and localization in spatially heterogeneous conditions, which may have important implications for triggered earthquakes and slow slip [24]. Finally, we acknowledge that fault zones have 3D structures. The current plane strain formulation can be extended to 3D in a straightforward way. However, the computational cost are orders of magnitude higher. We will report on our ongoing efforts in running a 3D implementation of our numerical method on the National Petascale Computing Facility Blue Waters [97,98] elsewhere.

VI. CONCLUSION

In this paper, we present a numerical model for shear defamation in gouge based on finite deformation kinematics and the shear transformation zone (STZ) viscoplasticity framework. Our numerical model generically predicts complex shear band localization patterns similar to what is reported in laboratory and field observations [8,9,99]. Our conclusions are summarized as follows:

(1) Complex strain localization patterns emerge, with minimum assumptions, including Riedel, boundary, and Y bands. The Riedel band follows the direction of the optimally oriented shear plane and emanates first from the initial disorder perturbation. With increased slip, the Y band starts to emerge and propagate. The boundary shear bands emerge due to the interaction of the Riedel shear and the sample boundaries.

(2) With increased dilatancy, the peak strength increases and the response becomes more brittle. At negligible dilatancy, the response is ductile and no shear bands form.

(3) With increased pressure, both the peak strength and the steady state flow stress increase. However, the response shows a brittle to ductile transition with increased pressure.

(4) With increased initial disorder (i.e., increased initial porosity), a brittle to ductile transition is also observed. For initially loose layers, the shear stress progressively increases toward the steady state value and the plastic deformation is distributed across the layer. For initially dense layers, the shear stress reaches a peak followed by strain softening and a complex shear band pattern emerges.

(5) The full development of the Riedel, boundary, and Y shears requires a sufficiently thick gouge layer. In a thin layer (where the thickness is of roughly the same magnitude as the initial perturbation), the plastic deformation is distributed across the layer and the response is ductile. With progressively increasing the layer thickness, at a constant imposed slip rate, the Riedel and Y bands develop.

ACKNOWLEDGMENTS

This research was funded by NSF/USGS Southern California Earthquake Center, funded through NSF Cooperative Agreement No. EAR0529922 and USGS Cooperative Agreement No. 07HQAG0008, and by grant from the National Science Foundation (CMMI-1435920). Additional funding was provided by the Center for Geologic Storage of CO2, an Energy Fronter Research Center funded by the U.S. Department of Energy (DOE), Office of Science, Basic Energy Sciences (BES), under Award No. DE-SC0C12504. The authors acknowledge access to Blue waters through Illinois Faculty Allocation Program. The Blue Waters sustained-petascale computing project, which is supported by the National Science Foundation (Awards No. OCI-0725070 and No. ACI-1238993) and the state of Illinois. Blue Waters is a joint effort of the University of Illinois at Urbana-Champaign and its National Center for Supercomputing Applications.

APPENDIX: STRESS (MATERIAL MODEL) UPDATE ALGORITHM

Here we describe the algorithm for the plastic strain rate and stress (material model) update in the Moose framework.

Algorithm 1: Stress (material model) update.

Algorithm 1: Stress (material model) update

for $t < t_{total}$ **do**
  At time $t = t_n$, χ_n, u_{x_n}, u_{y_n} are known
  Calculate $\dot{\chi}_n$, the total deformation gradient $\mathbf{F}_n$
  Calculate equivalent stress $\bar{s}$ and the yield strength s_0
  if $\bar{s} - s_0 > 0$ *(plasticity)* **then**
    Formulate the residual for each plastic strain rate: $R^i_{j+1} = \dot{\lambda}^i_j - \dot{\lambda}^i_{j+1}$
    while $|R| \geq tolerance$ **do**
      Formulate Jacobian: $jac = \frac{dR}{d\lambda}$
      Newton-Raphson Solve for $\dot{\lambda}^i_{j+1}$
      Update plastic deformation gradient: $\mathbf{F}^p$
      Update elastic deformation gradient: $\mathbf{F}^e = \mathbf{F}\mathbf{F}^{p^{-1}}$
      Update Cauchy-Green Strain tensor: $\mathbf{C}^e = \mathbf{F}^{e^T}\mathbf{F}^e$
      Update Green-Lagrangian Strain tensor: $\mathbf{E}^e = \frac{1}{2}(\mathbf{C}^e - \mathbf{I})$
      Update Pk2 Stress: $\mathbf{T} = \mathbf{L} : \mathbf{E}^e$
      Update Cauchy Stress: $\sigma = J^{e^{-1}}\mathbf{F}^e : \mathbf{T} : \mathbf{F}^{e^T}$
    end while
  else *elasticity*
    Update Pk2 Stress: $\mathbf{T} = \mathbf{L} : \mathbf{E}^e$
    Update Cauchy Stress: $\sigma = J^{e^{-1}}\mathbf{F}^e : \mathbf{T} : \mathbf{F}^{e^T}$
  end if
  Calculate the updated χ_{n+1}, the displacement $u_{x_{n+1}}$, $u_{y_{n+1}}$ through Residual equation

$$\mathbf{R} = \begin{bmatrix} R_\chi \\ R_u \end{bmatrix} = 0$$

  The terms in the Residual equations are provided to **Moose** through **Kernel**

$$R_\chi = \underbrace{\int_\Omega \dot{\chi}\phi dV}_{\text{HeatTimeDerivative Kernel}} - \underbrace{\int_\Omega (1 - \frac{\chi}{\hat{\chi}})(\frac{\mathbf{s} : \mathbf{D}^p_{dev}}{Pc_o})\phi dV}_{\text{HeatSource Kernel}}$$

$$R_u = \underbrace{\int_\Omega (\nabla \cdot \sigma)\phi dV}_{\text{Stress Divergence Kernel}} - \underbrace{\int_\Omega \rho\ddot{u}\phi dV}_{\text{Inertia Kernel}}$$

end for

[1] A.-M. Boullier, E.-C. Yeh, S. Boutareaud, S.-R. Song, and C.-H. Tsai, Microscale anatomy of the 1999 chi-chi earthquake fault zone, Geochem. Geophys. Geosyst. **10**, Q03016 (2009).

[2] F. M. Chester and J. S. Chester, Ultracataclasite structure and friction processes of the Punchbowl Fault, San Andreas system, California, Tectonophysics **295**, 199 (1998).

[3] N. De Paola, C. Collettini, D. R. Faulkner, and F. Trippetta, Fault zone architecture and deformation processes within evaporitic rocks in the upper crust, Tectonics **27**, TC4017 (2008).

[4] M. Fondriest, S. A. F. Smith, G. Di Toro, D. Zampieri, and S. Mittempergher, Fault zone structure and seismic slip localization in dolostones, an example from the Southern Alps, Italy, J. Struct. Geol. **45**, 52 (2012).

[5] V. Heesakkers, S. Murphy, and Z. Reches, Earthquake rupture at focal depth, part I: Structure and rupture of the Pretorius Fault, Tautona Mine, South Africa, Pure Appl. Geophys. **168**, 2395 (2011).

[6] S. A. F. Smith, A. Billi, G. Di Toro, and R. Spiess, Principal slip zones in limestone: Microstructural characterization and implications for the seismic cycle (Tre Monti Fault, Central Apennines, Italy), Pure Appl. Geophys. **168**, 2365 (2011).

[7] N. M. Beeler, T. E. Tullis, M. L. Blanpied, and J. D. Weeks, Frictional behavior of large displacement experimental faults, J. Geophys. Res.: Solid Earth **101**, 8697 (1996).

[8] J. M. Logan and B. Phenomena, Rev. Geophys. **17**, 1121 (1979).

[9] J. M. Logan, The progression from damage to localization of displacement observed in laboratory testing of porous rocks, Geol. Soc., London **289**, 75 (2007).
[10] C. Marone, Laboratory-derived friction laws and their application to seismic faulting, Annu. Rev. Earth Planet Sci. **26**, 643 (1998).
[11] C. Marone, C. B. Raleigh, and C. H. Scholz, Frictional behavior and constitutive modeling of simulated fault gouge, J. Geophys. Res.: Solid Earth **95**, 7007 (1990).
[12] A. P. Rathbun and C. Marone, Effect of strain localization on frictional behavior of sheared granular materials, J. Geophys. Res.: Solid Earth **115**, B01204 (2010).
[13] H. Kanamori and T. H. Heaton, Microscopic and macroscopic physics of earthquakes, in *Geocomplexity and the Physics of Earthquakes*, edited by J. B. Rundle, D. L. Turcotte, and W. Klein, Geophysical Monograph Series (American Geophysical Union, Washington, DC, 2013), pp. 147–163.
[14] J. R. Rice, Heating and weakening of faults during earthquake slip, J. Geophys. Res.: Solid Earth **111**, B05311 (2006).
[15] J. D. Platt, J. W. Rudnicki, and J. R. Rice, Stability and localization of rapid shear in fluid-saturated fault gouge: 2. Localized zone width and strength evolution, J. Geophys. Res.: Solid Earth **119**, 4334 (2014).
[16] J. R. Rice, J. W. Rudnicki, and J. D. Platt, Stability and localization of rapid shear in fluid-saturated fault gouge: 1. Linearized stability analysis, J. Geophys. Res.: Solid Earth **119**, 4311 (2014).
[17] E. G. Daub and J. M. Carlson, Stick-slip instabilities and shear strain localization in amorphous materials, Phys. Rev. E **80**, 066113 (2009).
[18] A. M. Hermundstad, E. G. Daub, and J. M. Carlson, Energetics of strain localization in a model of seismic slip, J. Geophys. Res.: Solid Earth **115**, 1 (2010).
[19] C. K. C. Lieou, A. E. Elbanna, J. S. Langer, and J. M. Carlson, Shear flow of angular grains: Acoustic effects and nonmonotonic rate dependence of volume, Phys. Rev. E **90**, 032204 (2014).
[20] K. R. Kothari and A. E. Elbanna, Localization and instability in sheared granular materials: Role of friction and vibration, Phys. Rev. E **95**, 022901 (2017).
[21] M. L. Falk and J. S. Langer, Dynamics of viscoplastic deformation in amorphous solids, Phys. Rev. E **57**, 7192 (1998).
[22] M. L. Falk and J. S. Langer, Deformation and failure of amorphous, solidlike materials, Annu. Rev. Condens. Matter Phys. **2**, 353 (2011).
[23] C. K. C. Lieou, A. E. Elbanna, and J. M. Carlson, Grain fragmentation in sheared granular flow: Weakening effects, energy dissipation, and strain localization, Phys. Rev. E **89**, 022203 (2014).
[24] C. K. C. Lieou, A. E. Elbanna, and J. M. Carlson, Dynamic friction in sheared fault gouge: Implications of acoustic vibration on triggering and slow slip, J. Geophys. Res.: Solid Earth **121**, 1483 (2016).
[25] J. H. Dieterich, Modeling of rock friction: 1. Experimental results and constitutive equations, J. Geophys. Res.: Solid Earth **84**, 2161 (1979).
[26] A. Ruina, Slip instability and state variable friction laws, J. Geophys. Res.: Solid Earth **88**, 10359 (1983).
[27] A. E. Elbanna and J. M. Carlson, A two-scale model for sheared fault gouge: Competition between macroscopic disorder and local viscoplasticity, J. Geophys. Res.: Solid Earth **119**, 4841 (2014).
[28] S. F. Edwards and R. B. S. Oakeshott, Theory of powders, Physica A **157**, 1080 (1989).
[29] C. K. C. Lieou and J. S. Langer, Nonequilibrium thermodynamics in sheared hard-sphere materials, Phys. Rev. E **85**, 061308 (2012).
[30] E. G. Daub and J. M. Carlson, A constitutive model for fault gouge deformation in dynamic rupture simulations, J. Geophys. Res.: Solid Earth **113**, B12309 (2008).
[31] E. G. Daub, M. L. Manning, and J. M. Carlson, Shear strain localization in elastodynamic rupture simulations, Geophys. Res. Lett. **35**, 1 (2008).
[32] M. L. Falk and J. S. Langer, From simulation to theory in the physics of deformation and fracture, MRS Bull. **25**, 40 (2000).
[33] M. L. Manning, E. G. Daub, J. S. Langer, and J. M. Carlson, Rate-dependent shear bands in a shear-transformation-zone model of amorphous solids, Phys. Rev. E **79**, 016110 (2009).
[34] M. L. Manning, J. S. Langer, and J. M. Carlson, Strain localization in a shear transformation zone model for amorphous solids, Phys. Rev. E **76**, 056106 (2007).
[35] A. Lemaître and J. Carlson, Boundary lubrication with a glassy interface, Phys. Rev. E **69**, 061611 (2004).
[36] E. G. Daub and J. M. Carlson, Friction, fracture, and earthquakes, Annu. Rev. Condens. Matter Phys. **1**, 397 (2010).
[37] J. S. Langer and M. L. Manning, Steady-state, effective-temperature dynamics in a glassy material, Phys. Rev. E **76**, 056107 (2007).
[38] C. K. C. Lieou, A. E. Elbanna, J. S. Langer, and J. M. Carlson, Stick-slip instabilities in sheared granular flow: The role of friction and acoustic vibrations, Phys. Rev. E **92**, 022209 (2015).
[39] B. Ferdowsi, M. Griffa, R. A. Guyer, P. A. Johnson, C. Marone, and J. Carmeliet, Three-dimensional discrete element modeling of triggered slip in sheared granular media, Phys. Rev. E **89**, 042204 (2014).
[40] B. A. Bilby, L. R. T. Gardner, and A. N. Stroh, Continuous distributions of dislocations and the theory of plasticity, in *Proceedings of the Nineth International Congress of Applied Mechanics, 1956* (Université de Bruxelles, Brussels, 1957), pp. 35–44.
[41] E. Kroner, *Kontinuumstheorie der Versetzungen und Eigenspannungen* (Springer, Berlin, 1958).
[42] E. H. Lee, Elastic-plastic deformation at finite strains, J. Appl. Mech. **36**, 1 (1969).
[43] L. Pechenik, Dynamics of shear-transformation zones in amorphous plasticity: Nonlinear theory at low temperatures, Phys. Rev. E **72**, 021507 (2005).
[44] J. S. Langer, Shear-transformation-zone theory of plastic deformation near the glass transition, Phys. Rev. E **77**, 021502 (2008).
[45] M. E. Gurtin, E. Fried, and L. Anand, *The Mechanics and Thermodynamics of Continua* (Cambridge University Press, Cambridge, UK, 2010).
[46] E. Bouchbinder and J. S. Langer, Nonequilibrium thermodynamics of driven amorphous materials. III. Shear-transformation-zone plasticity, Phys. Rev. E **80**, 031133 (2009).
[47] D. C. Drucker and W. Prager, Soil mechanics and plastic analysis or limit design, Q. Appl. Math. **10**, 157 (1952).

[48] D. L. Henann and K. Kamrin, A predictive, size-dependent continuum model for dense granular flows, Proc. Natl. Acad. Sci. USA **110**, 6730 (2013).
[49] Q. Zhang and K. Kamrin, Microscopic Description of the Granular Fluidity Field in Nonlocal Flow Modeling, Phys. Rev. Lett. **118**, 058001 (2017).
[50] D. Gaston, C. Newman, G. Hansen, and D. Lebrun-Grandié, Moose: A parallel computational framework for coupled systems of nonlinear equations, Nucl. Eng. Des. **239**, 1768 (2009).
[51] B. S. Kirk, J. W. Peterson, R. H. Stogner, and G. F. Carey, Libmesh: A C++ library for parallel adaptive mesh refinement/coarsening simulations, Eng. Comp. **22**, 237 (2006).
[52] S. Balay, S. Abhyankar, M. F. Adams, J. Brown, P. Brune, K. Buschelman, L. Dalcin, V. Eijkhout, W. D. Gropp, D. Kaushik *et al.*, PETSc, http://www.mcs.anl.gov/petsc.
[53] D. A. Knoll and D. E. Keyes, Jacobian-free Newton-Krylov methods: A survey of approaches and applications, J. Comput. Phys. **193**, 357 (2004).
[54] C. H. Rycroft and F. Gibou, Simulations of a stretching bar using a plasticity model from the shear transformation zone theory, J. Comput. Phys. **231**, 2155 (2012).
[55] B. M. Carpenter, D. M. Saffer, and C. Marone, Frictional properties of the active San Andreas fault at Safod: Implications for fault strength and slip behavior, J. Geophys. Res.: Solid Earth **120**, 5273 (2015).
[56] S. B. Giger, S. F. Cox, and E. Tenthorey, Slip localization and fault weakening as a consequence of fault gouge strengthening: Insights from laboratory experiments, Earth Planet. Sci. Lett. **276**, 73 (2008).
[57] S. H. Haines, B. Kaproth, C. Marone, D. Saffer, and B. van der Pluijm, Shear zones in clay-rich fault gouge: A laboratory study of fabric development and evolution, J. Struct. Geol. **51**, 206 (2013).
[58] A. Niemeijer, D. Elsworth, and C. Marone, Significant effect of grain size distribution on compaction rates in granular aggregates, Earth Planet. Sci. Lett. **284**, 386 (2009).
[59] C. Marone and C. H. Scholz, Particle-size distribution and microstructures within simulated fault gouge, J. Struct. Geol. **11**, 799 (1989).
[60] K. Mair and C. Marone, Friction of simulated fault gouge for a wide range of velocities and normal stresses, J. Geophys. Res.: Solid Earth **104**, 28899 (1999).
[61] A. R. Hinkle, C. H. Rycroft, M. D. Shields, and M. L. Falk, Coarse graining atomistic simulations of plastically deforming amorphous solids, Phys. Rev. E **95**, 053001 (2017).
[62] J. R. Rice, Inelastic constitutive relations for solids: An internal-variable theory and its application to metal plasticity, J. Mech. Phys. Solids **19**, 433 (1971).
[63] J. E. Andrade and R. I. Borja, Capturing strain localization in dense sands with random density, Int. J. Num. Methods Eng. **67**, 1531 (2006).
[64] R. I. Borja, Cam-clay plasticity, part V: A mathematical framework for three-phase deformation and strain localization analyses of partially saturated porous media, Comput. Methods Appl. Mech. Eng. **193**, 5301 (2004).
[65] R. I. Borja and J. E. Andrade, Critical state plasticity, part VI: Meso-scale finite element simulation of strain localization in discrete granular materials, Comput. Methods Appl. Mech. Eng. **195**, 5115 (2006).
[66] T. Poulet and M. Veveakis, A viscoplastic approach for pore collapse in saturated soft rocks using REDBACK: An open-source parallel simulator for Rock mEchanics with Dissipative feedBACK, Comput. Geotech. **74**, 211 (2016).
[67] J. R. Rice and J. W. Rudnicki, A note on some features of the theory of localization of deformation, Int. J. Solids Struct. **16**, 597 (1980).
[68] J. W. Rudnicki and J. R. Rice, Conditions for the localization of deformation in pressure-sensitive dilatant materials, J. Mech. Phys. Solids **23**, 371 (1975).
[69] J. R. Rice, N. Lapusta, and K. Ranjith, Rate and state-dependent friction and the stability of sliding between elastically deformable solids, J. Mech. Phys. Solids **49**, 1865 (2001).
[70] N. H. Sleep, E. Richardson, and C. Marone, Physics of friction and strain rate localization in synthetic fault gouge, J. Geophys. Res.: Solid Earth **105**, 25875 (2000).
[71] A. Le Bouil, A. Amon, S. McNamara, and J. Crassous, Emergence of Cooperativity in Plasticity of Soft Glassy Materials, Phys. Rev. Lett. **112**, 246001 (2014).
[72] C. E. Maloney and A. Lemaître, Amorphous systems in athermal, quasistatic shear, Phys. Rev. E **74**, 016118 (2006).
[73] P. Sollich, F. Lequeux, P. Hébraud, and M. E. Cates, Rheology of Soft Glassy Materials, Phys. Rev. Lett. **78**, 2020 (1997).
[74] L. Anand and C. Su, A constitutive theory for metallic glasses at high homologous temperatures, Acta Mater. **55**, 3735 (2007).
[75] A. S. Argon, Plastic deformation in metallic glasses, Acta Metall. **27**, 47 (1979).
[76] F. Spaepen, Homogeneous flow of metallic glasses: A free volume perspective, Scr. Mater. **54**, 363 (2006).
[77] B. Kondori, A. A. Benzerga, and A. Needleman, Discrete shear-transformation-zone plasticity modeling of notched bars, J. Mech. Phys. Solids **111**, 18 (2018).
[78] S. Urata and S. Li, A multiscale shear-transformation-zone (STZ) model and simulation of plasticity in amorphous solids, Acta Mater. **155**, 153 (2018).
[79] M. L. Manning and A. J. Liu, Vibrational Modes Identify Soft Spots in a Sheared Disordered Packing, Phys. Rev. Lett. **107**, 108302 (2011).
[80] S. Patinet, D. Vandembroucq, and M. L. Falk, Connecting Local Yield Stresses with Plastic Activity in Amorphous Solids, Phys. Rev. Lett. **117**, 045501 (2016).
[81] P. Segall and J. R. Rice, Dilatancy, compaction, and slip instability of a fluid-infiltrated fault, J. Geophys. Res.: Solid Earth **100**, 22155 (1995).
[82] N. H. Sleep, Frictional heating and the stability of rate and state-dependent frictional sliding, Geophys. Res. Lett. **22**, 2785 (1995).
[83] K. Kamrin and G. Koval, Nonlocal Constitutive Relation for Steady Granular Flow, Phys. Rev. Lett. **108**, 178301 (2012).
[84] S. R. Agnew and Ö. Duygulu, Plastic anisotropy and the role of non-basal slip in magnesium alloy AZ31b, Int. J. Plast. **21**, 1161 (2005).
[85] M. R. Barnett, A Taylor model based description of the proof stress of magnesium AZ31 during hot working, Metall. Mater. Trans. A **34**, 1799 (2003).
[86] A. S. Khan, A. Pandey, T. Gnäupel-Herold, and R. K. Mishra, Mechanical response and texture evolution of AZ31 alloy at large strains for different strain rates and temperatures, Int. J. Plast. **27**, 688 (2011).

[87] S. Kurukuri, M. J. Worswick, D. G. Tari, R. K. Mishra, and J. T. Carter, Rate sensitivity and tension–compression asymmetry in AZ31B magnesium alloy sheet, Philos. Trans. R. Soc. London, Ser. A **372**, 20130216 (2014).

[88] I. Ulacia, N. V. Dudamell, F. Gálvez, S. Yi, M. T. Pérez-Prado, and I. Hurtado, Mechanical behavior and microstructural evolution of a Mg AZ31 sheet at dynamic strain rates, Acta Mater. **58**, 2988 (2010).

[89] L. Anand and C. Gu, Granular materials: Constitutive equations and strain localization, J. Mech. Phys. Solids **48**, 1701 (2000).

[90] L. Anand and C. Su, A theory for amorphous viscoplastic materials undergoing finite deformations, with application to metallic glasses, J. Mech. Phys. Solids **53**, 1362 (2005).

[91] G. Di Toro, D. L. Goldsby, and T. E. Tullis, Friction falls towards zero in quartz rock as slip velocity approaches seismic rates, Nature (London) **427**, 436 (2004).

[92] G. Di Toro, R. Han, T. Hirose, N. De Paola, S. Nielsen, K. Mizoguchi, F. Ferri, M. Cocco, and T. Shimamoto, Fault lubrication during earthquakes, Nature (London) **471**, 494 (2011).

[93] R. Han, T. Shimamoto, T. Hirose, J.-H. Ree, and J.-I. Ando, Ultralow friction of carbonate faults caused by thermal decomposition, Science **316**, 878 (2007).

[94] T. Shimamoto and A. Tsutsumi, A new rotary-shear high-speed frictional testing machine: Its basic design and scope of research, J. Tectonic Res. Group Jpn. **39**, 65 (1994).

[95] N. J. Van Der Elst, E. E. Brodsky, P. Y. Le Bas, and P. A. Johnson, Auto-acoustic compaction in steady shear flows: Experimental evidence for suppression of shear dilatancy by internal acoustic vibration, J. Geophys. Res.: Solid Earth **117**, 1 (2012).

[96] B. Ferdowsi, M. Griffa, R. A. Guyer, P. A. Johnson, C. Marone, and J. Carmeliet, Acoustically induced slip in sheared granular layers: Application to dynamic earthquake triggering, Geophys. Res. Lett. **42**, 9750 (2015).

[97] B. Bode, M. Butler, T. Dunning, T. Hoefler, W. Kramer, W. Gropp, and W.-M. Hwu, The Blue Waters super-system for super-science, in *Contemporary High Performance Computing* (Chapman and Hall/CRC, Boca Raton, FL, 2013), pp. 339–366.

[98] W. Kramer, M. Butler, G. Bauer, K. Chadalavada, and C. Mendes, Blue Waters parallel I/O storage sub-system, in *High Performance Parallel I/O*, edited by Prabhat and Q. Koziol (CRC Press, Boca Raton, FL, 2015), pp. 17–32.

[99] D. R. Scott, C. J. Marone, and C. G. Sammis, The apparent friction of granular fault gouge in sheared layers, J. Geophys. Res.: Solid Earth **99**, 7231 (1994).

[100] J. E. Bowles, in *Foundation Analysis and Design* (McGraw-Hill Book, New York, 1982), p. 816.

[101] E. Bouchbinder and J. S. Langer, Nonequilibrium thermodynamics of driven amorphous materials. I. Internal degrees of freedom and volume deformation, Phys. Rev. E **80**, 031131 (2009).